Age and petrogenesis of the Andagul granodiorite and its implications on gold mineralization of the Kassan region, western Kyrgyzstan Tian Shan

Bo Zu[a], Chunji Xue[b,*], Guoxiang Chi[c], Nikolay Pak[d], Xiaobo Zhao[b], Xinli Wang[b]

[a] Faculty of Earth Resources, China University of Geosciences, Wuhan 4330074, China
[b] State Key Laboratory of Geological Processes and Mineral Resources, Faculty of Earth Sciences and Resources, China University of Geosciences, Beijing 100083, China
[c] Department of Geology, University of Regina, Regina, Saskatchewan S4S 0A2, Canada
[d] Institute of Geology, National Academy of Sciences, Bishkek 720040, Kyrgyzstan

ARTICLE INFO

ABSTRACT

A number of significant gold deposits in the Kassan region in west Kyrgyzstan are associated with the Andagul granitic intrusion. These gold deposits share similarities with the class of "intrusion-related gold deposits", implying that the gold mineralization may be genetically related to the intrusion. In order to evaluate this potential relationship, it is important to study the petrogenesis of the intrusion. This paper examines the sources and physiochemical conditions of magma generation and crystallization of the Andagul intrusion and their implications for gold mineralization, through an integrated study involving zircon geochronology, mineral chemistry, whole-rock chemistry and isotopic geochemistry. The Andagul intrusion consists mainly of granodiorite, which is characterized by metaluminous and median-K calc-alkaline compositions, high LREE and LILE, low HFSE, right-inclined REE pattern with a flat HREE pattern, and insignificant Eu anomalies (($Eu/Eu*)_N$ = 0.79–0.85). These geochemical characteristics, together with relatively low positive $\varepsilon_{Nd}(t)$ values (+2.1–+4.3), moderately low ($^{87}Sr/^{86}Sr)_i$ ratios (0.7049–0.7059), relatively low initial Pb isotopic ratios (($^{206}Pb/^{204}Pb)_t$ = 17.76–18.51, ($^{207}Pb/^{204}Pb)_t$ = 15.56–15.62, and ($^{208}Pb/^{204}Pb)_t$ = 37.89–38.33), juvenile $\varepsilon_{Hf}(t)$ (+2.29–+4.80) but relatively old model ages ($T_{2DM}(Hf)$ = 1026–1175 Ma, $T_{2DM}(Nd)$ = 728–907 Ma) indicate that the magma was mainly sourced from partial melting of juvenile basaltic lower crust with the involvement of a small proportion (ca. 5%–10%) of Precambrian basement rocks. The high Zr saturation temperatures (807 °C to 825 °C), relatively high $Mg^{\#}$ values (43–52) and presence of mafic enclaves, and development of acicular apatite and oscillatory plagioclase and titanite, suggest that the magmatism was related to injection of hot mantle material. The magma generation and intrusion took place during 299–310 Ma based on LA-ICPMS zircon U-Pb dating, suggesting a post-collisional setting. Remelting of sulfide accumulate residual with high Au/Cu ratios in the juvenile lower crust, formed in the pre-collisional plate subduction-related magmatic arc stage, is proposed to account for the Au mineralization in the Kassan region. The high water contents (4.0–5.2 wt% H_2O) and weakly oxidized or slightly reduced redox state (ΔFMQ = −0.33 ∼ +0.49) deduced from mineral composition and zircon Ce anomaly are favorable for the transport and enrichment of gold in the magmatic fluids. These geochemical characteristics suggest that the Andagul granodiorite and related granitic rocks in the Kassan region have the potential to provide ore-forming materials and fluids for gold mineralization.

1. Introduction

The Tian Shan metallogenic belt is well known for its endowment with voluminous giant and world-class gold deposits, which forms the world famous "Central Asian Gold Belt" (Fig. 1b) (Goldfarb et al., 2014; Xue et al., 2014; Yakubchuk et al., 2005). It is especially noteworthy that many of these gold deposits exhibit close temporal and spatial

relationship with Hercynian post-collisional intrusions, such as Muruntau (Morelli et al., 2007), Kumtor (Mao et al., 2004), Zarmitan (Abzalov, 2007), Jilau (Abzalov, 2007), Jerooy (Jenchuraeva and Oakes, 2001) and Unkurtash (Nikonorov et al., 2007), although it remains controversial whether or not gold and ore fluids were sourced from the igneous rocks (Abzalov, 2007; Cole et al., 2000; Morelli et al., 2007; Wall et al., 2004; Thompson and Newberry, 2000). In the last two
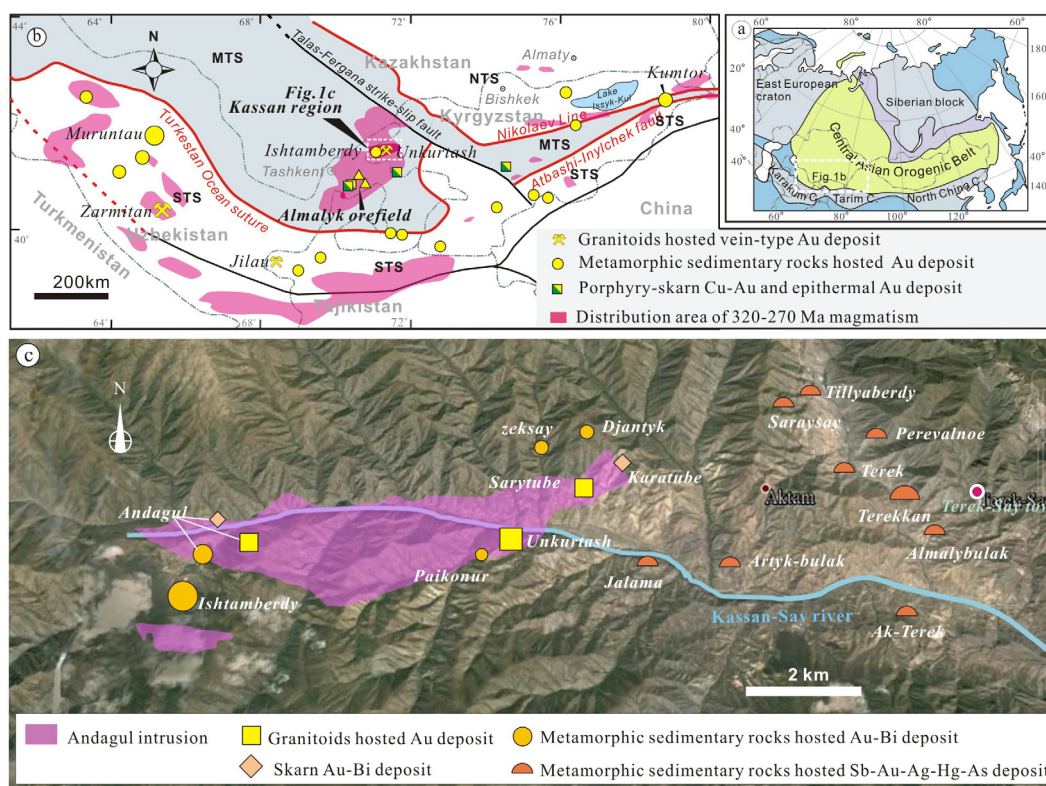

Fig. 1. (a) Principal tectonic zones and lineaments of Tian Shan orogenic belt showing the areas of granitoid magmatism from 320 to 270 Ma (Seltmann et al., 2011) and location of the major Au deposits (Goldfarb et al., 2014; Porter, 2006; Xue et al., 2014; Yakubchuk et al., 2005), (b) sketch tectonic map of the Kyrgyz Tian Shan showing the locations of the Kassan Au cluster and (c) distribution of the gold deposits around the Andagul granodiorite in Kassan Au cluster.

decades, the intrusion-related gold system has been treated as a separate group from orogenic deposits with the following peculiar characteristics: (1) tectonically located in a continental setting well inboard of convergent plate boundaries with tungsten and/or tin deposits (Lang and Baker, 2001; Baker and Lang, 2001); (2) a specific tectonic setting close to lithospheric boundaries and above previously metasomatized subcontinental lithospheric mantle (Mair et al., 2011; Groves et al., 2016); (3) a late- to post-collisional timing during transitional tectonic regimes (Mair et al., 2011; Fielding et al., 2018); (4) a spatial association with intrusions of intermediate to felsic compositions that lie near the boundary between ilmenite and magnetite series (Blevin, 2004; Bierlein, 2005); (5) zoning around a causative pluton, from sheeted gold veins in the intrusion cupola, to adjacent skarns, and to distal base metal-rich veins (Hart, 2007); and (6) pluton-proximal gold mineralization that may be associated with elevated Bi, Te, while W aureole-hosted mineralization may have an As or Sb tenor, and distal mineralization that may be related to elevated Ag-Sb-Pb-Zn concentrations (Nevolko et al., 2018). Considering the potential genetic link between the gold mineralization and granitic intrusions, it is of vital importance to decipher the sources, emplacement history, and physiochemical conditions of crystallization for the gold-related intrusions. Even though considerable geochronology and geochemistry research has been conducted on the Hercynian granites in the Tian Shan (Dolgopolova et al., 2017; Gou et al., 2012; Konopelko et al., 2007; Solomovich, 2007), few of them focus on the gold-related intrusions and discuss the factors that facilitate gold mineralization.

The Kassan region, located in the western part (Chatkal range) of the Kyrgyz Tian Shan, is endowed with dozens of gold deposits or occurrences (Fig. 1c; Nikitin, 1997; Nikonorov et al., 2007), including Unkurtash (125t Au), Ishtamberdy (110t Au), Andagul (21t Au), Karatube (5t Au), Terek (21t Au), Saraysay-Tillyaberdy (17t Au), Terekkan (8t Au), and Karatube (5t Au). These deposits are characterized by a wide range of mineralization styles and metal associations that vary in

concentric zones outward from the Andagul granitic intrusion, including intrusion-hosted Au (W) deposits, skarn Au-Bi deposits, metamorphic rock hosted Au-Bi deposits to distal Sb-Au-Ag-Hg-As deposits. This spatial distribution pattern of gold mineralization styles resembles typical magmatic-hydrothermal mineralization systems documented elsewhere (Hart, 2007; Sillitoe and Bonham, 1990; Thompson and Newberry, 2000), implying that the gold mineralization in the Kassan region may be genetically related to the Andagul intrusion. The Unkurtash gold deposit, which is characterized by occurrence of sheeted quartz vein arrays, and the Karatube skarn deposit that is hosted by or occurs immediately adjacent to the granite intrusions and its metamorphic aureole, are particularly similar to intrusion-related gold deposits (Lang and Baker, 2001; Hart, 2007). Thus, the research on petrogenesis of the Andagul intrusion is a pivotal component in deciphering the genesis of gold mineralization in the Kassan region, with potential impact for selection and validation of exploration models.

In this contribution, we present a systematic geochemical dataset, including mineral chemistry, zircon LA-ICPMS geochronology, whole-rock geochemistry and Sr-Nd-Pb-Hf isotopic data, on the Andagul intrusion. These data are used to investigate the magma source(s), magmatic processes and physico-chemical conditions including water content and redox state, which are important parameters that decide whether or not an intrusion is fertile (Hart, 2007; Sillitoe and Bonham, 1990; Thompson and Newberry, 2000). The significance of the study results for intrusion-related gold mineralization in the Tian Shan metallogenic belt in general is discussed.

2. Geological setting

2.1. Tectonic framework

The 2500 km long E-W trending Tian Shan in the southern margin of

the Central Asian Orogenic Belt (CAOB) (Fig. 1a) has been subdivided into North-, Middle- and South Tian Shan by the Nikolaev Line and the Turkestan Ocean suture-Atbashi-Inylchek Faults (Fig. 1b). These fault zones represent Paleozoic sutures of the Terskey and Turkestan Oceans, respectively (Biske et al., 2013; Seltmann et al., 2011).

The North Tian Shan (NTS) is a collage of several Precambrian microcontinental fragments and lower Paleozoic continental arcs, amalgamated and stitched by granite intrusions during the Cambrian and Ordovician (Alexeiev et al., 2016; Windley et al., 2007), and is tectonically regarded as the deformed margin of the Paleo-Kazakhstan continent. The Middle Tian Shan (MTS) west of the Talas-Fergana fault is composed of the late Paleozoic Beltau-Kurama volcano-plutonic arc formed on Precambrian basement, early Paleozoic shallow and deep marine sedimentary sequences and middle Paleozoic arc-related magmatic rocks as a result of the northward subduction of the Turkestan Ocean (Fig. 1b) (Loury et al., 2016; Seltmann et al., 2011). The South Tian Shan (STS) is a Late Paleozoic accretionary complex and comprises a pile of folded tectonic nappes and thrust structures formed due to convergence and collision of the Kazakhstan continent in the north with the Karakum-Tarim continents in the south (Fig. 1b) (Alexeiev et al., 2017).

The Chatkal-Kurama terrane of the Middle Tian Shan, where the study area is located, was formed on the northern margin of the Turkestan Ocean during the Middle and Late Paleozoic in response to northward subduction of the Turkestan Ocean (Seltmann et al., 2014; Yakubchuk et al., 2005). It is characterized by two discrete short lived subduction-related volcano-plutonic series of Silurian-Early Devonian and Late Carboniferous ages, separated by Middle Devonian to Early Carboniferous carbonate sequences (Alexeiev et al., 2016; Konopelko et al., 2017). The first impulse of arc magmatism from Silurian to Middle Devonian formed andesite, dacite, rhyolites and tuffs stitched by alkali-calcic granites and leucogranites with ages ranging from 420 to 390 Ma (Alexeiev et al., 2016; Biske et al., 2013; Konopelko et al., 2017; Seltmann et al., 2011). The subduction resumed in the Pennsylvanian and resulted in a thick (up to 5–6 km) sequence of andesitic volcanic and volcanogenic-terrigenous strata in the Chatkal-Kurama area of the MTS, later intruded by Andean-type intrusions (Biske et al., 2013; Burtman, 2015). Dating of volcanic complexes and intrusions in the Chatkal-Kurama region yielded ages in the range of 320–280 Ma (Fig. 1b), suggesting that subduction-related Carboniferous magmatism was, possibly without interruption, followed by the emplacement of post-collisional complexes (Konopelko et al., 2017; Seltmann et al., 2011).

2.2. Late Paleozoic magmatism and mineralizations

The Late Paleozoic (320–270 Ma) granitoid intrusions, extensively distributed in the Tian Shan (Fig. 1b), have been broadly subdivided into subduction-related and post-collisional categories (Dolgopolova et al., 2017; Seltmann et al., 2011). The subduction-related intrusions are clustered in the Chatkal-Kurama segment of the Middle Tian Shan (Fig. 1b), and are represented by calc-alkaline volcanic arc magmas that formed due to the resume of northward subduction of the oceanic crust of the Turkestan Ocean (Dolgopolova et al., 2017; Käßner et al., 2017; Seltmann et al., 2011). This episode of magmatism is closely associated with formation of the giant Almalyk porphyry Cu-Au cluster (e.g. Kalmakyr, Dalnee, Sarycheku, Kyzata, Kyzylalma, Kochbulak, Kauldy deposits) in the Kurama arc (Fig. 1b)(Dolgopolova et al., 2017; Käßner et al., 2017; Seltmann et al., 2011).

In contrast to the subduction-related intrusions, which are restricted to the Chatkal-Kurama region, the post-collisional magmatism affected the whole region across terrane boundaries (Fig. 1b) and comprises compositionally diverse magmatic series (Konopelko et al., 2007; Seltmann et al., 2011). The eastern part of the STS is characterized by widely developed A-type, locally rapakivi-textured, granites and related greisen-type Sn-W mineralization, whereas the western STS and most

part of the MTS (including the Chatkal-Kurama range) are featured with potassium alkali-calcic granites and minor calc-alkaline rocks (Konopelko et al., 2007; Solomovich, 2007). In a few cases post-collisional granitoids are associated with mafic and/or silica undersaturated alkaline rocks and peraluminous S-type granites (Seltmann et al., 2011).

Metallogeny of the post-collisional intrusions is characterized by the development of intrusion-related Au deposits, Au skarns, orogenic Au deposits and greisen-type Sn-W deposits (Seltmann et al., 2011). The gold deposits associated with the post-collisional granites in this region include some of the largest economic gold accumulations in the world, e.g. Muruntau, Kumtor, Zarmitan and Amantaitau (Fig. 1b) (Goldfarb et al., 2014; Xue et al., 2014; Yakubchuk et al., 2005). Most of these gold deposits are associated with calc-alkaline I-type granites or granodiorites, located within the intrusions or their contact metamorphic aureoles, and yield isotopic ages of mineralization similar to the host magmatism (Abzalov, 2007; Cole et al., 2000; Morelli et al., 2007; Thompson and Newberry, 2000; Wall et al., 2004).

3. Geology of the Kassan region and the Andagul intrusion

3.1. Geology of the Kassan region

The Kassan region is geographically located in the southeast of the Chatkal range in the western Kyrgyzstan Tian Shan (Fig. 1b), and represents the westernmost segment of the Middle Tian Shan microcontinent juxtaposed to the South Tian Shan thrust-and-fold belt along the South Tian Shan Suture zone (Mühlberg et al., 2016). The Kassan region in the Chatkal range is mainly made of metamorphic rocks and Paleozoic volcanic and sedimentary sequences intruded by Carboniferous and Early Permian granites and granodiorites (Fig. 2) (Bakirov et al., 2003; Nikitin, 1997).

The metamorphic rocks of the Chatkal Range consist of the tectonically lower Shaldyr, Tereksai and Semyzsay units and the upper Ishtamberdy unit (Fig. 2), which were initially assumed to register a Neo- to Meso-Proterozoic continental basement (Alexeiev et al., 2016; Bakirov et al., 2003) and recently reinterpreted as a Paleozoic protolith superimposed by Late Carboniferous eclogite metamorphic event (Loury et al., 2016; Mühlberg et al., 2016). The Shaldyr, Tereksai and Semyzsay units are exposed as an antiform consisting of schist, paragneiss, marble, amphibolitie facies volcanic and volcano-sedimentary rocks in the western part of the Kassan region (Fig. 2). These three units are bounded by low- to medium-grade metamorphosed sandstones and schists of the Ishtamberdy unit, which is overlain by adjacent unmetamorphosed Paleozoic rocks with fault contacts (Bakirov et al., 2003).

The lower Paleozoic sequences consist of carbonaceous slate, andesitic basalt and tuff of the Early Silurian age and andesite, trachyandesitic tuff, breccias and conglomerate of the Early Devonian age. Passive margin formations of Middle to Late Devonian ages occupy a significant part of the area with thick sandstone, siltstone, marl, limestone, dolomite, gypsum, and slate. Recurrent volcanic rocks are documented elsewhere with Pennsylvanian arc-related volcanic and siliciclastic rocks developed in the Chatkal Region beyond Fig. 2 (Alexeiev et al., 2016; Mühlberg et al., 2016). The youngest formations are Late Carboniferous to Early Permian sedimentary and volcanic rocks that are scattered in the southeast of the area with dominantly volcanic breccia, andesite and tuff interbedded with conglomerate and sandstone (Fig. 2).

The above metamorphic and sedimentary rocks are intruded by two undeformed intrusions, named Zeksay and Andagul, respectively (Fig. 2). The Zeksay intrusion was previously assumed to be of Neoproterozoic age, but later on, multigrain $^{207}Pb/^{206}Pb$ ages of 464 ± 8 and 420 ± 20 Ma were obtained with the evaporation method (Bakirov et al., 2003). Recently, zircon dating of coarse-grained K-feldspar-biotite granite and diorite from the Zeksay intrusion yielded Early
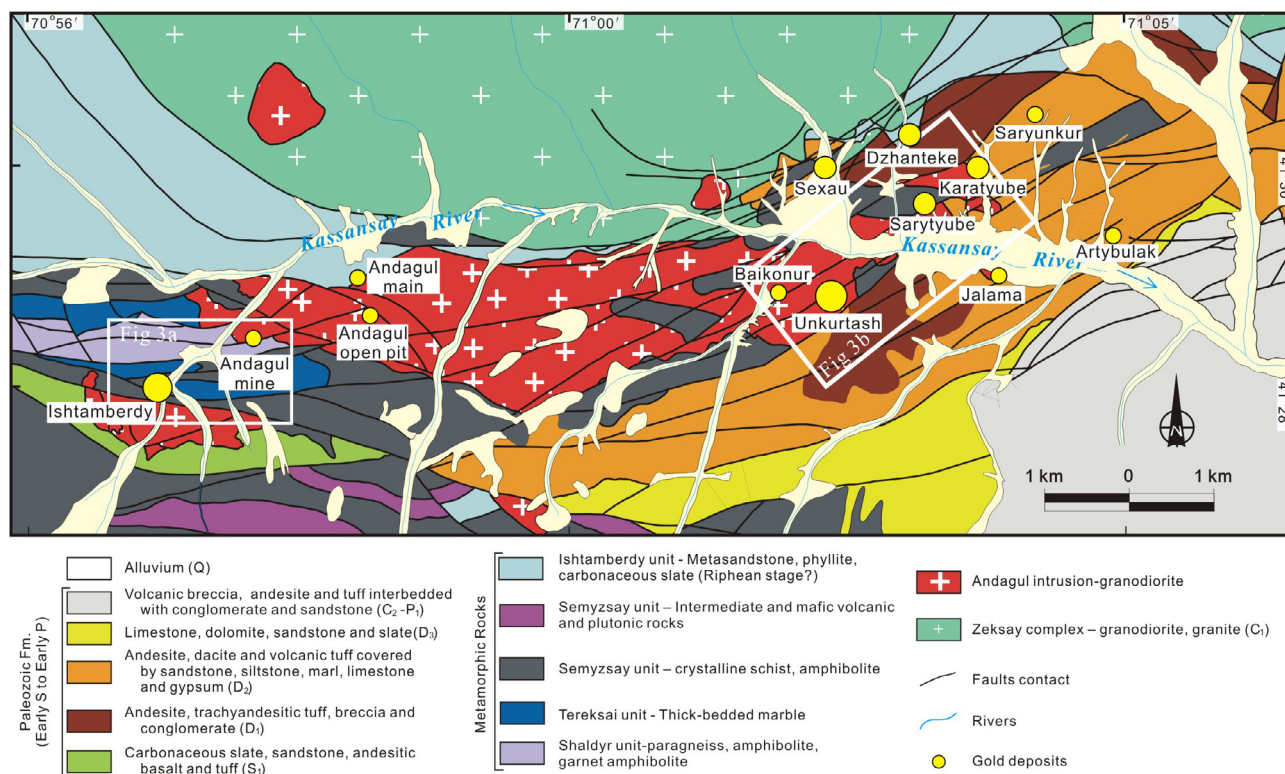
Fig. 2. Geological characteristics of the Andagul granodiorite and gold deposits in the Kassan region (Nikitin, 1997).

Carboniferous ages of 322 ± 2 Ma and 329 ± 3 Ma (Alexeiev et al., 2016), corresponding to the early phase of arc magmatism. The Andagul granodiorite, however, has not been well constrained with geochronology and geochemistry.

Multiple faults are developed in the region and cut the above described geological units. All the geologic boundaries exhibit fault contact with each other with significant displacement (Fig. 2c). These faults can be roughly grouped into two arrays trending northwest-southeast and northeast-southwest, respectively. The two fault arrays crosscut each other, suggesting roughly contemporaneous activity possibly linked to a northward compression against the relatively rigid Zeksay complex. The intersection nodes of these two arrays of faults appear to have controlled the Andagul intrusion and gold mineralization in the region (Fig. 2) (Kudrin et al., 1990).

3.2. Gold mineralization and its relationship with the Andagul intrusion

The Kassan region is impregnated with numerous gold deposits and occurrences that are either hosted by or adjacent to the Andagul granodiorite (Fig. 1c), including granitoid hosted Au deposits (Unkurtash, Sarytube), skarn Au-(As-Bi) deposit (Karatube), metamorphic sedimentary rocks hosted Au-(As-Bi) deposit (Ishtamberdy) and distal Sb-Au-Ag-Hg-As deposit (Terekkan, Terek, Artyk-Bulak).

The Unkurtash Au deposit located in the east of the Kassan region is hosted by the Andagul granodiorite (Fig. 3b). The Unkurtash deposit has geological characteristics typical of the intrusion-related gold deposits (Hart, 2007; Lang and Baker, 2001), including (1) intrusion-hosted, sheeted arrays of quartz veins (Fig. 3c–d), (2) comparatively restricted hydrothermal alteration confined to narrow envelop along the veins (Fig. 3e), (3) CH_4-bearing carbonic hydrothermal fluids, (4) metal assemblage that combines gold with W, As, Mo, Te and low concentrations of Cu, Pb, Zn, (5) a low sulfide content (less than 5%) with a reduced ore mineral assemblage that comprises arsenopyrite, pyrrhotite and pyrite and lacks magnetite or hematite and (6) a continental setting well inboard of convergent plate boundaries (Fig. 1b).

Re-Os dating with molybdenite from the Unkurtash gold deposits yields an age of 307.6 ± 1.5 Ma for the gold mineralization.

The Karatube skarn Au-(As-Bi) deposit occurs in the contact zone between the Andagul intrusion and adjacent limestone, shale and gypsum formations (Fig. 3b) (Nikonorov et al., 2007). The intrusion and country rocks are intensively altered to a thick zone (up to 40 m) of skarns and hornfels with pervasively developed chlorite, actinolite, diopside superimposed on garnet and pyroxene (Fig. 3f). Gold mineralization is confined to the skarn zones and shows close association with skarn minerals and metallic minerals (Fig. 3g) including pyrite, chalcopyrite, arsenopyrite, magnetite, hematite and tennantite.

The large Ishtamberdy Au-As deposit located about 0.5 km from the Andagul intrusion (Fig. 3a), is hosted by schist and amphibolite-schist of the Semyzsay unit. The host rocks form an asymmetric anticline with marble in the core and quartz-feldspar-biotite and amphibolite schist on the flanks (Nikonorov et al., 2007). Orebodies of the Ishtamberdy deposit are mainly controlled by interbedding fracture zones and delamination zones of the anticline and to a lesser extent by high angle fault zones crosscutting the south flank of the anticline. The orebodies are morphologically divided into saddle-shaped bodies in the core, steeply dipping tabular concordant bodies and steeply dipping intersecting bodies in fault zones. Individual orebodies consist of auriferous quartz-sulfide veins and veinlets that are parallel or sub-parallel to the fractures and deformed beddings (Fig. 3h). The main ore minerals include pyrite, arsenopyrite, gold and minor antimonite, chalcopyrite, sphalerite, pyrrhotite, tetrahedrite, hematite, galena and scheelite (Nikonorov et al., 2007). Locally gold mineralization is developed in skarn (Fig. 3a), which may represent a distal skarn developed in fractures linked to the Andagul intrusion (Xue et al., 2014).

The Terekkan Au-Sb deposit is situated in the east of the Kassan region, together with the Tereksay Sb and Artyk-Bulak Hg-Au-Ag deposits and several other medium to small deposits with Sb-Ag-Hg assemblage (Fig. 1c). The gold mineralization of the Terekkan Au-Sb deposit is confined within the crystalline schist of the Semyzsay unit that underwent hydrothermal alteration (Nikonorov et al., 2007). The
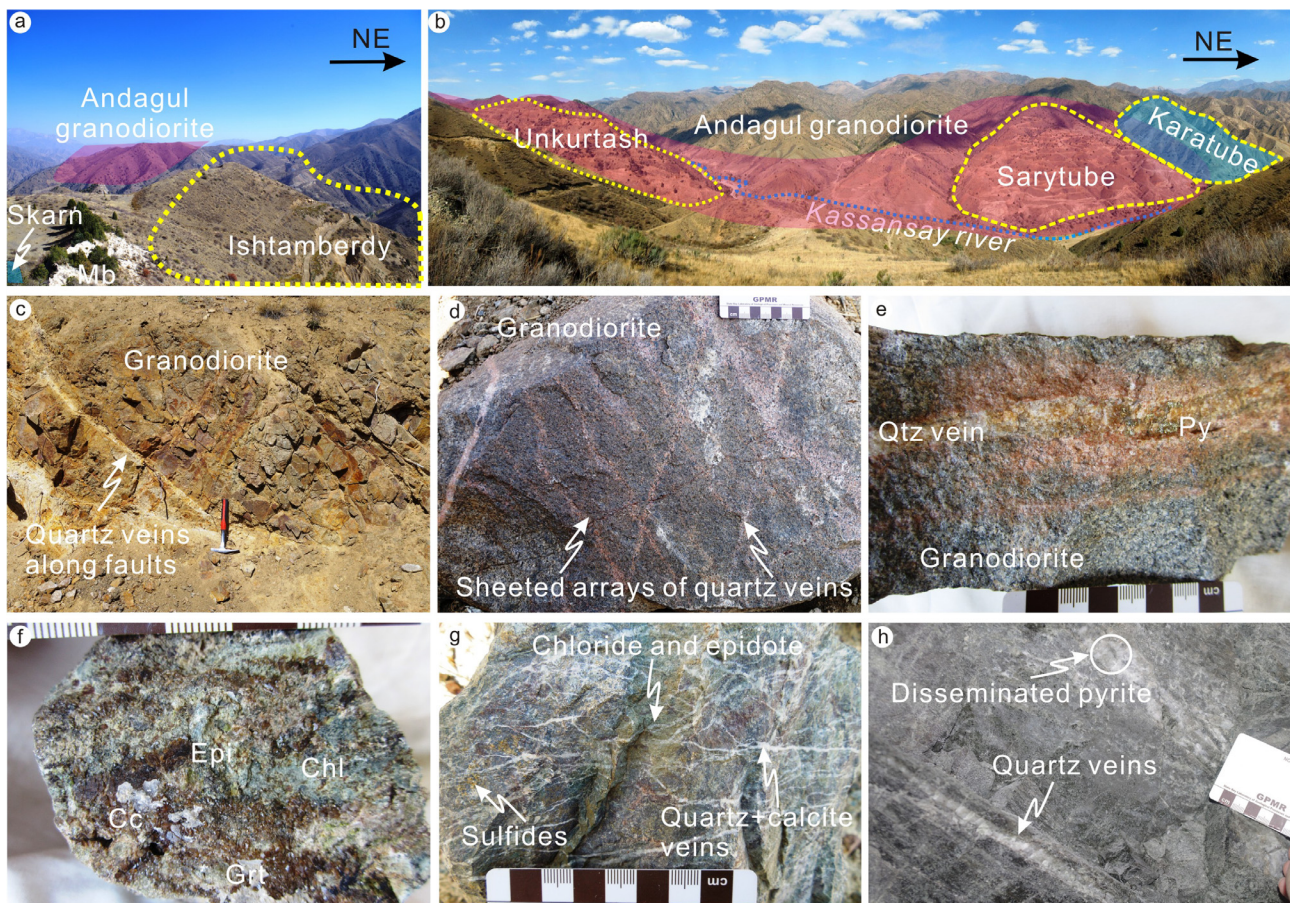
Fig. 3. Location of the gold deposits (Ishtamberdy, Unkurtash, Sarytube, Karatube) relative to the Andagul granodiorite in the western part (a) and eastern part (b) showing a closely spatial relationship. The dashed lines outline the deposit area relatively to the Andagul granodiorite in a and b. The red shadow areas roughly represent the location of the Andagul granodiorite, whereas the light blue shadow outline the skarn alteration area in Karatube deposit area (b) and little in the Ishtamberdy area (a). (c)–(e) show typical gold mineralization in the Unkurtash gold deposits: (c). quartz veins developed along the faults that crosscutting the granodiorite; (d). sheeted arrays quartz veins in the granodiorite are typical ore features; (e). gold mineralization developed in the quartz veins and narrow enveloped alteration along the veins. (f)–(g) show typical skarn mineralization in the Karatube gold deposits: (f). early formed garnets are overprinted with chlorite, epidote and calcite; (g). gold and sulfide precipitated with the formation of chlorite and epidote and then are crosscut by the quartz-calcite veins. (h). typical quartz vein ores in the schist from the Ishtamberdy deposit. (For interpretation of the references to color in this figure legend, the reader is referred to the web version of this article.)

gold mineralization is characterized by quartz veins accompanied by beresitization along steep faults. The orebodies are steeply dipping (mainly to NE) or subhorizontal. The main metallic minerals include gold, pyrite, arsenopyrite, antimonite, pyrrhotite, with minor chalcopyrite, sphalerite and magnetite.

Even though diverse mineralization characteristics are developed in the Kassan region, gold deposits are associated with the Andagul intrusion (Fig. 1c). The gradual change of metal associations and mineralization characteristics of these deposits outward from the Andagul intrusion (Fig. 1c) may be ascribed to the decreasing temperature away from the intrusion, resembling typical intrusion-related gold systems established elsewhere (Hart 2007; Lang and Baker 2001; Thompson and Newberry 2000).

3.3. Petrography of the Andagul granodiorite

The Andagul intrusion is generally outcropped as an east–west striking, wedge-like body with an exposed area of about 10 km^2 (Fig. 1c). The elongation of the intrusion coincides with the structure fabric of the surrounding metamorphic and sedimentary rocks (Fig. 2). Detailed field survey reflects that the lithology of the Andagul intrusion is dominated by granodiorite with rare quartz diorite along its margins.

The Andagul granodiorite is characterized by light grayish brown color, massive structure and typical medium-grained granitic texture

(Fig. 4b). It is composed of plagioclase (c. 55 vol%), quartz (c. 15 vol%), K-feldspar (c. 10 vol%), and amphibole (c. 10 vol%) with abundant biotite (c. 5 vol%) and minor accessory minerals (less than 5 vol%). Plagioclase often forms large, euhedral crystals of 0.5 to 3 mm length with well-developed polysynthetic twin and rhythmic zonation (Fig. 4g and h). Abundant apatite, K-feldspar and magnetite inclusions are common in the plagioclase (Fig. 4g and h). K-feldspar grains are commonly euhedral to subhedral whilst quartz grains and ragged plates of green-brown biotite occur as interstitial phases (Fig. 4d and g). Biotite is a common mineral in the Andagul granodiorite and varies in morphology from euhedral tabular to subhedral blade-shaped crystals (Fig. 4d and e) with weak chloritization (Fig. 4e). Amphibole occurs as euhedral to subhedral crystals and is 0.05–1.0 mm in length with abundant mineral inclusions such as apatite and magnetite (Fig. 4d–f).

Apatite occurs ubiquitously as euhedral and laths inclusions within amphibole, plagioclase, zircon and as groundmass intergranular grains (Fig. 4e–i). Inclusions of acicular apatite length to width ratios of 10:1 in the plagioclase are also common (Fig. 4h). Titanite crystals are typically in euhedral rhombus form with well-preserved oscillatory zonings (Fig. 4i). Magnetite is common in the Andagul granodiorite and some is included in amphibole as rounded grains (Fig. 4f and i). Rutile, monazite and scheelite are also present (Fig. 4f and i).

The Andagul granodiorite contains a small quantity (less than 3% in volume) darker colored diorite enclaves with plagioclase crystals
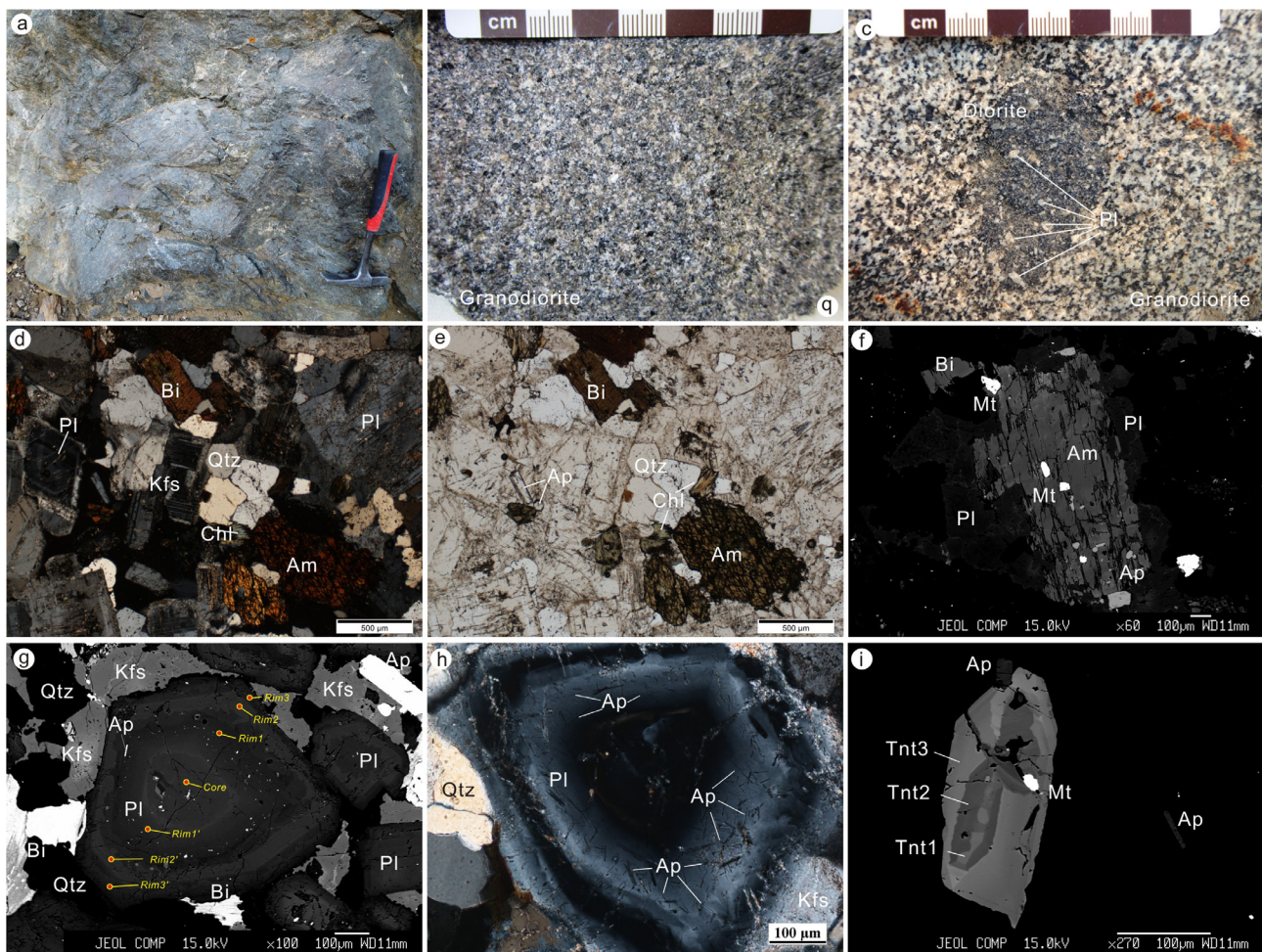
Fig. 4. a. Outcrop photograph of the Andagul granodiorite in the western part of the Kassan region; b. fresh granodiorite samples with massive texture and grey color; c. diorite enclaves show crenulated contact with granodiorite host and contain heterogeneous scattered plagioclase xenocrysts; d and e. thin sections photomicrographs of a representative granodiorite sample; f. amphibole with magnetite and apatite inclusions; g. Plagioclase with well-developed polysynthetic twin and rhythmic zonation, note the red dots represent EPMA analyze location (Sample 18–3); h. Inclusions of acicular apatite in the plagioclase mantle; i. Euhedral shape titanite with well-preserved core-mantle-rim zonings (Am, amphibole; Ap, apatite; Bi, biotite; Chl, chlorite; Kfs, K-feldspar; Mt, magnetite; Pl, plagioclase; Qtz, quartz; Tnt, titanite). (For interpretation of the references to color in this figure legend, the reader is referred to the web version of this article.)

straddling the boundaries (Fig. 4c). The Andagul granodiorite shows clearly intrusive contacts with its country rocks with sharp and chilled margins. The country rocks vary from metamorphic schists, amphibolite, genesis and marble mainly in the west to sandstone, siltstone, gypsum, marl, limestone in the east (Fig. 2), with the development of thick skarn alteration zones locally (Fig. 3f–g). Xenoliths of sedimentary rocks are common and show variable reaction with the Andagul granodiorite.

4. Sampling and analytical techniques

Representative fresh granodiorite of the Andagul intrusion were sampled both in outcrops in the west part of the intrusion (Fig. 4a; sample UN-16 to 21) and in a prospecting adit near the Unkurtash deposit in the east part of the intrusion (sample UN-67 to 74; Fig. 1c). The samples show fairly uniform lithology and mineral composition. Thin sections from these samples were examined for petrography and for assuring the freshness of the samples for geochemical studies.

4.1. Mineral chemistry

The major element compositions of plagioclase, K-feldspar, hornblende, biotite and magnetite were analyzed with Electron Micro-Probe Analyzer (EMPA) at the State Key Laboratory of Geological Processes and Mineral Resources, China University of Geosciences (Wuhan), with a JEOL JXA-8100 EPMA equipped with four wavelength-dispersive spectrometers (WDS). An accelerating voltage of 15 kV, a beam current of 20 nA and a 10 μm spot size were used to analyze the minerals. Results are given in Tables 1–4.

4.2. LA-ICP-MS U-Pb dating and REE distribution in zircon

Zircons for LA-ICP-MS (Laser Ablation Inductively Coupled Plasma Mass Spectrometry) U-Pb dating were extracted using conventional heavy liquid and magnetite separation techniques and then handpicked under a binocular microscope. Internal morphology was examined with transmitted and reflected light microscopes as well as cathodoluminescence (CL) images prior to *in situ* U-Pb and Hf isotopic analyses.

Simultaneous *in situ* measurement of U-Pb ages and trace elements of zircons with LA-ICP-MS were conducted using a Finnigan Neptune inductively coupled plasma mass spectrometry that connected to a NewWave UP-213 laser ablation at the Institute of Mineral Resources, Chinese Academy of Geological Sciences (CAGS). All analyses were carried out using a beam spot size of ca. 35 μm and a laser frequency of 10 HZ and energy density about 2.5 J/cm^2. Helium was applied as a

Table 1
The average values of Plagioclase and K-feldspar in the Andagul granodiorite (wt%).

	18-2-1	18-2-2	18-2-3	18-2-4	18-3-1	18-3-2	18-3-3	18-3-4	18-3-5	18-3-6	18-3-7	18-3-8	69-2-1
	Plagioclase, 18-2				Plagioclase, 18-3								
	Core	Rim1	Rim2	Rim3	Rim3	Rim2	Rim1	Core	Rim1′	Rim2′	Rim3′		
SiO_2	55.11	59.45	56.67	65.08	60.75	58.85	61.45	58.36	61.03	58.38	61.33	66.01	65.59
TiO2	0.01	0.00	0.00	0.00	0.00	0.00	0.02	0.01	0.00	0.00	0.00	0.02	0.01
Al_2O_3	28.70	25.72	27.32	22.33	25.19	26.26	24.59	26.59	24.96	26.35	24.37	18.27	18.57
Fe_2O_3	0.25	0.25	0.26	0.18	0.08	0.17	0.12	0.20	0.09	0.15	0.19	0.11	0.12
FeO	0.00	0.00	0.00	0.00	0.00	0.00	0.00	0.00	0.00	0.00	0.00	0.00	0.00
MnO	0.01	0.00	0.02	0.00	0.00	0.02	0.00	0.00	0.01	0.02	0.02	0.02	0.00
MgO	0.00	0.01	0.00	0.01	0.00	0.01	0.01	0.01	0.00	0.00	0.00	0.00	0.00
CaO	11.13	7.83	9.95	3.97	6.93	8.40	6.43	8.54	6.62	8.44	6.12	0.02	0.06
Na_2O	4.85	6.59	5.43	8.78	7.40	6.44	7.56	6.40	7.14	6.17	7.69	1.22	1.59
K_2O	0.15	0.27	0.20	0.41	0.17	0.19	0.42	0.30	0.35	0.20	0.19	15.01	14.16
Total	100.20	100.12	99.85	100.77	100.52	100.33	100.58	100.39	100.20	99.71	99.91	100.68	100.11
Si	4.96	5.30	5.10	5.70	5.38	5.24	5.44	5.21	5.40	5.22	5.45	6.03	6.00
Al	3.04	2.70	2.90	2.30	2.63	2.76	2.56	2.79	2.60	2.78	2.55	1.97	2.00
Fe^{3+}	0.02	0.02	0.02	0.01	0.01	0.01	0.01	0.01	0.01	0.01	0.01	0.01	0.01
Fe^{2+}	0.00	0.00	0.00	0.00	0.00	0.00	0.00	0.00	0.00	0.00	0.00	0.00	0.00
Ti	0.00	0.00	0.00	0.00	0.00	0.00	0.00	0.00	0.00	0.00	0.00	0.00	0.00
Mn	0.00	0.00	0.00	0.00	0.00	0.00	0.00	0.00	0.00	0.00	0.00	0.00	0.00
Mg	0.00	0.00	0.00	0.00	0.00	0.00	0.00	0.00	0.00	0.00	0.00	0.00	0.00
Ca	1.07	0.75	0.96	0.37	0.66	0.80	0.61	0.82	0.63	0.81	0.58	0.00	0.01
Na	0.85	1.14	0.95	1.49	1.27	1.11	1.30	1.11	1.23	1.07	1.33	0.22	0.28
K	0.02	0.03	0.02	0.05	0.02	0.02	0.05	0.03	0.04	0.02	0.02	1.75	1.65
Ab	44	59	49	78	65	58	66	57	65	56	69	11	15
An	55	39	50	20	34	41	31	42	33	43	30	0	0
Or	1	2	1	2	1	1	2	2	2	1	1	89	85

Table 2
Representative electron microprobe analysis data (wt.%) of biotite in the Andagul granodiorite.

Sample No.	18-3-9	18-4-1	69-1-1	69-2-2	18-5-2	18-5-3
SiO_2	36.85	37.30	37.18	37.24	37.04	37.67
TiO_2	3.87	4.32	5.03	4.76	4.20	4.58
Al_2O_3	13.87	13.96	13.89	14.05	13.52	13.89
FeO	22.06	16.62	22.46	21.05	19.36	18.00
MnO	0.50	0.48	0.33	0.33	0.44	0.46
MgO	9.57	12.76	8.68	10.31	11.42	12.33
CaO	0.00	0.00	0.03	0.00	0.00	0.00
Na_2O	0.09	0.16	0.11	0.08	0.09	0.13
K_2O	9.06	9.14	8.93	8.93	9.03	9.21
F	0.19	0.68	0.03	0.13	0.38	0.38
Cl	0.08	0.08	0.11	0.11	0.08	0.09
Number of ions on the basis of 22 oxygens						
Si	5.65	5.61	5.66	5.62	5.64	5.63
Al^{IV}	2.35	2.39	2.34	2.38	2.36	2.37
Al^{VI}	0.16	0.09	0.15	0.12	0.07	0.07
Ti	0.45	0.49	0.58	0.54	0.48	0.51
Fe^{3+}	0.51	0.61	0.62	0.58	0.55	0.57
Fe^{2+}	2.32	1.48	2.24	2.07	1.92	1.68
Mn	0.06	0.06	0.04	0.04	0.06	0.06
Mg	2.19	2.86	1.97	2.32	2.59	2.75
Ca	0.00	0.00	0.01	0.00	0.00	0.00
Na	0.03	0.05	0.03	0.02	0.03	0.04
K	1.77	1.75	1.73	1.72	1.75	1.76
Total	15.49	15.39	15.38	15.42	15.45	15.43
$Fe^{2+}/(Mg + Fe)$	0.46	0.30	0.46	0.42	0.38	0.34
T (°C)	710	747	741	740	732	748
Si	5.65	5.61	5.66	5.62	5.64	5.63

external standard. Raw data reduction was performed off-line using Isoplot/ver.4.1.5 (Ludwig, 2003). Individual analyses for U-Pb isotopes and REE are presented with 1σ errors in Tables 5 and 6 and uncertainties in age results are quoted at the 95% confidence level.

4.3. Zircon Hf isotope

Zircon *in situ* Hf isotope (Table 7) analyses was measured in previously U-Pb dated zircons, using a Neptune multi-collector ICP-MS equipped with a New Wave UP213 laser-ablation microprobe at Institute of Mineral Resources, CAGS. The isobaric interference of ^{176}Lu on ^{176}Hf was corrected using a recommended $^{176}Lu/^{175}Lu$ ratio of 0.02669 to calculate $^{176}Lu/^{177}Hf$. In order to correct the isobaric interferences of ^{176}Yb on ^{176}Hf, the $^{176}Yb/^{172}Yb$ value of 0.5886 and mean β_{Yb} value obtained during Hf analysis on the same spot. During the course of this study, zircons GJ-1 was used as the reference standards with a laser repetition rate of 10 HZ at 100 mJ and the laser beam diameters of 40 μm. The $\varepsilon_{Hf}(t)$ value was calculated by assuming chondritic ratios of $^{176}Lu/^{177}Hf$ (0.282772) and $^{176}Hf/^{177}Hf$ (0.0332). The single model ages (T_{DM}) were calculated using the measured $^{176}Lu/^{177}Hf$ ratios of zircon, based on the assumption that the depleted mantle reservoir is 0.28325 at present and $^{176}Lu/^{177}Hf$ ratio are 0.0384 (Griffin et al., 2002). The two-stage model age (T_{DM2}) was calculated for the source rocks of magma using mean $^{176}Lu/^{177}Hf$ value of 0.015 for the average continental crust (Griffin et al., 2002).

4.4. Whole-rock chemistry and Sr-Nd-Pb isotopes study

Fresh granodiorite samples for elemental and isotopic analyses were first trimmed and chipped and then powdered in an agate mill to about 200 mesh for analyzing. The major elements were analyzed using X-ray Fluorescence (XRF) at the Institute of Geology and Geophysics, Chinese Academy of Sciences, Beijing. The analytical precision and accuracy for most major elements measured are generally better than 5%. FeO was analyzed by the titration method with standard deviation less than 10 percent. Analyses of trace element, including rare earth elements, were undertaken at the National Research Center of Geoanalysis, CAGS,

carrier gas to efficiently transport the aerosol materials. Zircon 91,500 and GJ-1 was used as an external standard to correct for instrumental mass discrimination and elemental fractionation with every 5 analyses. $^{207}Pb/^{206}Pb$ and $^{206}Pb/^{238}U$ ratios were calculated using the *ICPMSDataCal* program and then corrected using the Harvard zircon 91,500 as external standard. The U, Th and Pb concentrations were calibrated using ^{29}Si as an internal standard and NIST SRM 610 as an

Table 3
Representative electron microprobe analysis data (wt%) of amphibole in the Andagul granodiorite.

Spot		18-1-1	69-1-2	69-2-3	69-3-1	18-5-6
SiO_2		49.19	47.48	47.49	45.96	50.82
TiO_2		0.94	1.11	1.12	1.39	0.68
Al_2O_3		5.47	6.64	6.80	7.87	4.76
Cr_2O_3		0.00	0.00	0.00	0.00	0.00
FeO		12.19	16.09	16.66	16.49	11.86
MnO		0.79	0.76	0.79	0.70	0.81
MgO		15.59	12.77	12.54	11.96	15.93
CaO		11.00	10.39	10.56	10.85	11.15
Na_2O		1.07	1.39	1.34	1.43	1.07
K_2O		0.47	0.64	0.67	0.74	0.38
F		–	–	–	–	–
Cl		–	–	–	–	–
Total		96.71	97.27	97.96	97.39	97.45
Number of ions on the basis of 13 cations						
T	Si	7.07	6.91	6.89	6.75	7.24
	Al^{IV}	0.93	1.09	1.11	1.25	0.76
	Ti	0.00	0.00	0.00	0.00	0.00
C	Al^{VI}	0.00	0.05	0.05	0.12	0.03
	Cr	0.00	0.00	0.00	0.00	0.00
	Fe^{3+}	0.96	1.04	1.04	0.86	0.82
	Ti	0.10	0.12	0.12	0.15	0.07
	Mg	3.34	2.77	2.71	2.62	3.38
	Fe^{2+}	0.50	0.92	0.99	1.16	0.60
	Mn	0.10	0.09	0.10	0.09	0.10
B	Fe^{2+}	0.00	0.00	0.00	0.00	0.00
	Ca	1.69	1.62	1.64	1.71	1.70
	Na	0.15	0.19	0.18	0.15	0.15
A	Na	0	0.01	0.02	0.12	0.00
	K	0	0.12	0.12	0.14	0.07
$Mg/(Mg + Fe^{2+})$		0.87	0.75	0.73	0.69	0.85
$Al^{\#}(Al^{VI}/Al^{tot})$		0.00	0.05	0.04	0.08	0.04
T (°C)		765	771	774	810	738
[a]P (Kbar)			1.22	1.25	1.23	
[a]Calculated depth (km)			4.51	4.63	4.56	
[b]P (Kbar)		0.73	0.99	1.02	1.36	0.61
[b]Calculated depth (km)		2.7	3.7	3.8	5.0	2.3
H_2O_{melt} (wt%)		4.0	4.7	4.8	5.2	4.1

Note: ①[a]P is calculated from the equation of Anderson and smith, (1995). Only three data fulfill the requirement of the equation.
②[b]P is calculated from thermo-barometric equations of Ridolfi et al. (2010).
③Depth is calculated assuming average density of 2.7 g/cm³ for the upper crust.

Table 4
Electron microprobe analysis data (wt%) of magnetite in the Andagul granodiorite.

Sample No.	69-2-4	18-2-5
FeO	31.12	31.18
Fe_2O_3	69.17	69.30
Na_2O	0.02	–
K_2O	–	–
MnO	0.04	0.07
MgO	–	–
CaO	0.03	–
Al_2O_3	0.06	0.13
TiO_2	0.10	0.20
SiO_2	0.08	0.04
Total	100.60	100.92

Beijing, using an ICP-MS (X-series). Rhodium was used as an internal standard to monitor signal drift during counting. The analytical error is generally less than 5% for trace elements. The geochemical data are presented in Table 8.

The concentrations and isotopic ratios of Sm, Nd, Rb, Sr, U, Th and Pb were determined using a VG354 thermal ionization mass spectrometer at the Modern Analysis Center, Nanjing University. The mass fractionation corrections for Sr and Nd isotopic ratios are based on

Table 5
LA-ICP-MS U-Pb geochronology results of zircons from the Andagul granodiorite.

Spot no.	Pb (μ g/g)	Th²³² (μ g/g)	U²³⁸ (μ g/g)	Th/U	Isotopic ratios								Apparent age (Ma)							
					$^{207}Pb/^{206}Pb$	1σ	$^{207}Pb/^{235}U$	1σ	$^{206}Pb/^{238}U$	1σ	$^{208}Pb/^{232}Th$	1σ	$^{207}Pb/^{206}Pb$	1σ	$^{207}Pb/^{235}U$	1σ	$^{206}Pb/^{238}U$	1σ	$^{208}Pb/^{232}Th$	1σ
Un-67-1	24	165	393	0.50	0.05777	0.00216	0.37984	0.01498	0.04751	0.00077	0.01469	0.00050	520	88	327	11	299	5	295	10
Un-67-2	13	69	212	0.42	0.05619	0.00217	0.37302	0.01538	0.04788	0.00082	0.01382	0.00063	461	85	322	11	301	5	277	13
Un-67-3	13	99	202	0.32	0.05178	0.00225	0.34797	0.01527	0.04855	0.00081	0.01411	0.00058	276	100	303	12	306	5	283	12
Un-67-4	16	157	242	0.49	0.05462	0.00221	0.36451	0.01483	0.04859	0.00076	0.01413	0.00054	398	91	316	11	306	5	284	11
Un-67-5	13	112	213	0.65	0.05511	0.00222	0.37060	0.01586	0.04863	0.00082	0.01390	0.00054	417	91	320	12	306	5	279	11
Un-67-6	14	90	230	0.53	0.05290	0.00218	0.35324	0.01483	0.04864	0.00084	0.01436	0.00064	324	94	307	11	306	5	288	13
Un-67-7	32	305	510	0.39	0.05567	0.00162	0.37216	0.01113	0.04865	0.00067	0.01435	0.00050	439	65	321	8	306	4	288	10
Un-67-8	22	161	346	0.60	0.05293	0.00217	0.35634	0.01521	0.04886	0.00082	0.01376	0.00050	324	93	309	11	307	5	276	10
Un-67-9	21	176	323	0.47	0.05380	0.00198	0.36072	0.01318	0.04888	0.00091	0.01445	0.00051	361	83	313	10	308	6	290	10
Un-67-10	22	158	341	0.55	0.05254	0.00172	0.35547	0.01219	0.04889	0.00087	0.01434	0.00051	309	76	311	9	308	5	288	10
Un-67-11	15	73	234	0.46	0.05323	0.00188	0.35833	0.01339	0.04892	0.00095	0.01511	0.00061	339	80	315	10	308	6	303	12
Un-67-12	25	211	387	0.31	0.05445	0.00192	0.36378	0.01239	0.04900	0.00083	0.01421	0.00047	391	84	307	9	308	5	285	9
Un-67-13	23	147	380	0.54	0.05255	0.00188	0.35347	0.01244	0.04905	0.00065	0.01493	0.00064	309	77	308	9	309	4	300	13
Un-67-14	18	184	277	0.39	0.05214	0.00163	0.35406	0.01178	0.04911	0.00069	0.01471	0.00051	300	70	305	9	309	4	295	10
Un-67-15	18	147	296	0.67	0.05164	0.00182	0.34985	0.01355	0.04911	0.00079	0.01452	0.00056	333	81	305	10	309	5	291	11
Un-67-16	22	151	359	0.50	0.05160	0.00180	0.35009	0.01258	0.04913	0.00068	0.01430	0.00062	333	80	305	9	309	4	287	12
Un-67-17	17	135	270	0.42	0.05423	0.00231	0.36662	0.01547	0.04930	0.00073	0.01488	0.00053	389	94	317	11	310	4	299	10

Table 6
LA-ICP-MS analytical results of trace elements (in ppm) in zircons of the Andagul granodiorite.

Spot	La	Ce	Pr	Nd	Sm	Eu	Gd	Tb	Dy	Ho	Er	Tm	Yb	Lu	Y	Th	U	Hf	[a]Eu_N/Eu_N^*	[a]Ce/Ce^*	[b]T(°C)	[c]log fO₂	[c]FMQ
UN-67-1	0.51	19.83	0.13	1.34	3.45	0.97	10.38	3.70	50.23	20.96	105.36	26.03	283.41	65.05	687.21	160.52	554.39	9007.17	0.50	3.24	711	-16.83	0.01
UN-67-2	0.01	21.15	0.02	0.79	2.56	0.58	7.35	3.25	41.89	17.58	93.65	23.49	261.91	60.67	591.89	201.05	561.86	8427.60	0.41	7.76	660	-18.02	0.22
UN-67-3	0.06	20.31	0.18	2.03	3.58	0.67	7.62	2.63	33.92	14.66	76.84	18.87	208.79	49.75	481.64	174.35	529.94	8938.13	0.39	1.64	646	-18.42	0.21
UN-67-4	0.01	16.93	0.04	0.44	1.51	0.56	4.93	1.82	23.04	9.62	50.78	12.64	147.03	32.26	311.50	182.82	530.97	9072.11	0.62	10.36	709	-17.18	-0.28
UN-67-5	0.06	12.82	0.02	0.39	1.66	0.42	4.24	1.59	20.52	8.84	48.51	12.66	140.00	33.92	303.50	100.47	310.13	8090.20	0.48	8.51	703	-17.21	-0.17
UN-67-6	0.20	17.02	0.10	0.84	2.42	0.78	7.73	2.83	37.16	15.64	81.30	20.17	220.73	52.00	512.81	124.41	442.05	8796.81	0.55	5.10	714	-16.80	-0.03
UN-67-7	1.93	22.93	0.38	1.95	2.45	0.63	6.39	2.32	30.83	13.12	66.74	16.90	189.77	44.64	431.00	184.58	576.60	9018.68	0.49	2.66	667	-17.74	0.30
UN-67-8	0.15	17.87	0.04	0.51	3.29	0.67	8.36	2.93	37.73	15.31	78.17	18.69	205.97	46.58	502.26	172.86	583.04	8900.65	0.39	6.68	625	-19.27	0.00
UN-67-9	0.02	14.92	0.07	0.85	2.39	0.68	5.69	2.10	25.00	11.15	55.17	13.85	180.36	36.98	353.49	180.36	444.73	7573.79	0.56	3.50	740	-16.44	-0.31
UN-67-10	0.01	12.50	0.01	0.27	1.40	0.36	4.32	1.61	21.24	9.63	50.72	13.12	155.35	36.76	321.95	89.78	322.30	8994.87	0.44	14.30	689	-17.68	-0.25
UN-67-11	1.87	21.06	0.46	2.23	2.99	0.53	6.80	2.47	29.86	13.38	69.57	17.20	192.11	44.07	446.41	155.73	398.77	7658.66	0.36	1.64	693	-16.82	0.49
UN-67-12	0.01	11.98	0.01	0.44	1.60	0.37	4.50	1.46	19.06	8.33	43.42	10.95	124.46	29.77	278.46	109.96	324.73	7891.20	0.42	6.39	711	-17.19	-0.33
UN-67-13	0.01	19.27	0.03	0.31	1.92	0.52	5.55	2.00	26.60	11.23	60.26	15.01	168.09	40.26	382.07	203.54	616.75	8737.81	0.49	16.20	659	-18.29	-0.03
UN-67-14	0.09	19.90	0.06	0.69	2.71	0.81	9.42	3.20	39.10	16.59	83.10	19.99	219.55	49.79	550.20	200.55	605.29	8202.77	0.49	6.37	698	-17.19	0.01
UN-67-15	0.07	18.63	0.02	0.24	1.73	0.41	5.05	2.07	25.82	11.25	57.03	14.49	164.58	37.53	372.07	213.43	600.96	8669.78	0.42	20.38	676	-17.91	-0.12
UN-67-16	0.03	17.88	0.03	0.42	2.36	0.61	7.05	2.40	31.14	13.90	71.85	17.52	195.19	45.36	445.94	163.92	483.47	8450.65	0.45	10.37	713	-16.84	-0.05
UN-67-17	0.06	29.86	0.06	1.06	3.51	0.83	10.95	4.00	50.16	21.75	110.48	27.09	295.38	68.33	705.48	325.05	858.54	9444.58	0.41	6.87	684	-17.28	0.28

[a] Note: $Eu_N/Eu_N^* = Eu_N/(Sm_N^*Gd_N)^{1/2}$, and the Ce/Ce^* was calculated using lattice strain model.

[b] Ti-in-zircon temperatures are calculated using the equation proposed by Ferry and Watson (2007).

[c] Oxygen fugacity was calculated by the methods of Smythe and Brenan (2016).

$^{86}Sr/^{88}Sr = 0.1194$ and $^{146}Nd/^{144}Nd = 0.7219$, respectively. The $^{87}Sr/^{86}Sr$ ratio of the standard NBS 987 and $^{143}Nd/^{144}Nd$ ratio of the standard La Jolla were 0.710233 ± 6 (2σ) and 0.511863 ± 6 (2σ), respectively (Table 9). Overall blank contributions are less than 1 ng for Sr and less than 60 pg for Nd. Pb was separated and purified using a conventional AG50 1-×8 anion-exchange technique with diluted HBr as eluant. Pb isotope analyses were performed on a Finnigan MAT Triton TI thermal ionizing mass spectrometer (TIMS). The $^{208}Pb/^{204}Pb$, $^{207}Pb/^{204}Pb$ and $^{206}Pb/^{204}Pb$ ratios of the NBS-981 standard were 36.715 ± 9 (1σ), 15.487 ± 11 (1σ) and 16.941 ± 8 (1σ), respectively (Table 9).

5. Analytical results

5.1. Mineralogy and mineral chemistry

The analyzed plagioclase in the Andagul granodiorite show a range of SiO₂ contents from 58.36 to 61.45 wt%, Al₂O₃ contents from 24.37 to 26.59 wt%, CaO contents from 6.12 to 8.54 wt%, K₂O contents from 0.17 to 0.42 wt%, Fe₂O₃ contents from 0.08 to 0.20 wt%. The calculated An (anorthite) contents in plagioclase varies from An20 to An55, belonging to oligoclase and andesine (Table 1). Petrographic observation reveals that the plagioclase is commonly featured with well-developed polysynthetic twin and rhythmic zonation. Line profile analyses of two plagioclase grains show that An contents decrease from 42 to 55% in the core, to 31–39% in the thick inner mantle (rim 1), increase to 41–50% in the outer mantle (rim2) and then decrease to 20–34% (rim3), displaying significant compositional oscillatory (Fig. 5a and b). The contents of CaO, Al₂O₃ and Fe₂O₃ correlate positively with An whereas the contents of SiO₂, K₂O, Na₂O show a reverse trend (Table 1).

The analytical results show that K-feldspars contain little CaO (0.02%-0.06%). They have high contents of Or (orthoclase, 85–89 wt %), minor Ab (albite, 11–15 wt%) and negligible An component (Table 1).

The analyzed biotite are all primary biotite without significant alteration or re-equilibration using the discrimination diagram of 10 * TiO₂ - (FeO + MnO)-MgO (Fig. 5c) (Nachit et al., 2005). All the analyzed biotite has less than 0.55 Ti atoms per formula unit normalized to 22O atoms and $Fe^{2+}/(Mg + Fe)$ ratios are all clustered in a small range (0.30–0.46), pertaining to fresh magmatic biotite (Li et al., 2017). All the biotites analyzed are classified as Mg-biotite and ferrobiotite with Mg/(Mg + Fe) ratios (atomic) ranging from 0.77 to 1.37 (Fig. 5d). Most of the analyzed grains are enriched in F rand Cl (Fig. 5e) with F/(F + Cl) ratios of 0.55 to 0.89 except one with 0.19 (Table 2).

The analyzed hornblende grains are commonly poor in F and Cl contents (Table 3) and are characterized by enrichment of magnesium with $Mg^{2+}/(Fe^{2+} + Mg^{2+})$ ratios ranging from 0.69 to 0.87 (Fig. 5f) (Leake et al., 1997). The Al₂O₃ contents are less than 8 wt%.

Magnetite is nearly pure Fe₃O₄ with less than 2% of ulv spinel (Fe₂TiO₄) component (Table 4).

5.2. Zircon U-Pb ages

Zircons grains recovered from the Andagul granodiorite are euhedral to subeuhedral and display long prismatic crystals (150–300 μm) with an aspect ratio of 2:1 to 4:1 (Fig. 6a). They are transparent or yellowish in transmitted light with apparent oscillatory zoning on CL images (Fig. 6a). All the 17 analyses on zircon grains yield concordant or near-concordant $^{206}Pb/^{238}U$ ages between 299 and 310 Ma (Table 5) with a mean of 306.9 ± 2.3 Ma (2σ, MSWD = 0.35, n = 17) (Fig. 6a).

5.3. Zircon trace elements

The 17 trace element analyses for LA-ICPMS zircon grains display similar total REE abundances, from 217 to 624 ppm (Table 6). Their chondrite-normalized patterns (Fig. 6b) are characterized by steeply

Table 7
Zircon Lu–Hf isotope data for the Andagul granodiorite.

No.	$^{176}Hf/^{177}Hf$	± 1σ	$^{176}Yb/^{177}Hf$	± 1σ	$^{176}Lu/^{177}Hf$	± 1σ	T(Ma)	$\epsilon_{Hf(0)}$	$\epsilon_{Hf(t)}$	$f_{Lu/Hf}$	T_{DM1}(Ma)	T_{DM2}(Ma)
1	0.282676	0.000012	0.019	0.000295	0.000740	0.000010	299	−3.41	3.01	−0.98	812	1124
2	0.282682	0.000013	0.015	0.000125	0.000585	0.000004	301	−3.17	3.33	−0.98	799	1105
3	0.282692	0.000013	0.023	0.000211	0.000912	0.000007	306	−2.81	3.72	−0.97	792	1084
4	0.282652	0.000012	0.023	0.000141	0.000878	0.000005	306	−4.25	2.29	−0.97	848	1175
5	0.282712	0.000011	0.019	0.000289	0.000741	0.000009	306	−2.10	4.47	−0.98	760	1036
6	0.282719	0.000012	0.017	0.000141	0.000653	0.000004	306	−1.88	4.72	−0.98	749	1021
7	0.282696	0.000012	0.019	0.000303	0.000735	0.000010	306	−2.69	3.89	−0.98	783	1074
8	0.282708	0.000011	0.016	0.000274	0.000627	0.000009	308	−2.27	4.36	−0.98	764	1045
9	0.282674	0.000011	0.020	0.000246	0.000797	0.000009	308	−3.46	3.14	−0.98	815	1123
10	0.282685	0.000013	0.028	0.000252	0.001086	0.000007	308	−3.08	3.47	−0.97	806	1102
11	0.282720	0.000012	0.015	0.000088	0.000615	0.000004	309	−1.86	4.80	−0.98	748	1017
12	0.282716	0.000013	0.018	0.000164	0.000712	0.000006	309	−1.98	4.67	−0.98	754	1026
13	0.282713	0.000013	0.021	0.000148	0.000835	0.000004	309	−2.10	4.52	−0.97	762	1036
14	0.282707	0.000012	0.017	0.000346	0.000647	0.000011	309	−2.28	4.38	−0.98	765	1045
15	0.282695	0.000011	0.015	0.000186	0.000586	0.000005	310	−2.71	3.99	−0.98	781	1070

rising slopes REE patterns with $(La/Yb)_N$ lower than 0.030, indicating a significant HREE enrichment relative to LREE. They also exhibit remarkable positive Ce and negative Eu anomalies (Fig. 6b). The Eu anomaly values of zircon grains range from 0.33 to 0.62 by a conventional method based on normalized values of Sm and Gd concentrations. The calculation of Ce^{4+}/Ce^{3+} ratios follows the method proposed by (Ballard et al., 2002), where the abundance of Ce^{3+} is determined from the REE concentrations and whole-rock data on the basis of a lattice-strain model for mineral-melt partition of elements. The calculated Ce^{4+}/Ce^{3+} ratios of the Andagul granodiorite range from 1.64 to 20.38 (Table 6), lower than the calculated Ce^{4+}/Ce^{3+} ratios of the porphyry Cu related granodiorite in the Almalyk region with an average of 53.96.

5.4. Zircon Hf isotopic compositions

The Hf isotope analyses on 15 zircons (Table 7) from Andagul granodiorite show very low $^{176}Lu/^{177}Hf$ ratios within the range from 0.00059 to 0.00109. The $^{176}Hf/^{177}Hf$ ratios fall in a narrow range from 0.28265 to 0.28272 (Fig. 7a) with corresponding $\epsilon_{Hf}(0)$ values from −4.25 to −1.86. The initial ϵ_{Hf} values ($\epsilon_{Hf}(t)$) of these zircons have a consistent, small calculated values ranging from +2.29 to +4.80 (Fig. 7b) and far away from those of the Early Paleoproterozoic crust of Northern Tarim (Long et al., 2012). They also display $f_{Lu/Hf}$ of -0.98 to -0.97, and T_{2DM} of 1026 to 1175 Ma.

5.5. Whole-rock geochemistry

Major and trace elemental compositions of the Andagul granodiorite are shown in Table 8. The LOI is less than 1.29 wt% (except one sample 12Un-21 at 2.66 wt%) and shows no apparent correlation with the major or trace elements (Table 8), suggesting that alteration (if present) is minor and the analytical results reflect the primary composition of the granodiorite. The Andagul granodiorite samples have a narrow range of SiO_2 contents from 61.07 to 65.04 wt% and show subalkaline characteristics, with K_2O of 1.66–2.80 wt%, Na_2O of 3.62–4.04 wt% and total alkalis ($Na_2O + K_2O$) of 5.28–6.66%. In the TAS ($Na_2O + K_2O$ vs. SiO_2) (Fig. 8a) and K_2O-SiO_2 (Fig. 8b) diagrams, all the samples are plotted into the subalkaline granodiorite and median K calc-alkaline series field, respectively, reveling an overall medium-K calc-alkaline character. They also exhibit relatively high contents of Al_2O_3 (16.10–17.19 wt%) and CaO (4.41–5.41 wt%) and display metaluminous characteristics (Fig. 8c) with low aluminum saturation index of A/CNK ($Al_2O_3/(CaO + Na_2O + K_2O)$ mol.) and A/NK ($Al_2O_3/(Na_2O + K_2O)$ mol.) (Table 8). The samples have moderate concentrations of FeO (2.80–4.60 wt%) and MgO (1.44–2.33 wt%) with high values of $Mg^\#$ ($Mg^\# = 100 \times$ molar $MgO/(MgO + FeO, 43–52)$,

overlapping with the geochemical classification of the magnesian granitoids and different from the widely distributed Early-Permian A-type granites in the STS (Fig. 8d).

The granodiorite samples are also characterized by significant enrichment in LREEs ($La_N = 242–265$) and relatively flat to concave-up MREE to HREEs($(Dy/Yb)_N = (1.01–1.34)$, $(Gd/Yb)_N = 1.6–1.8$) patterns, with strong fractionation between light and heavy REE ($(La/Yb)_N = 11.1–12.5$). They do not show any marked Eu anomalies ($(Eu/Eu^*)_N = 0.79–0.85$) (Fig. 9a). On the primitive mantle-normalized spider diagrams (Fig. 9b), all the samples exhibit consistent trace elemental patterns, with elevated abundances of light REE and large-ion lithophile elements (LILE; K, Ba, Sr) as well as Th, U and Pb). They are also characterized by pronounced negative anomalies of high field strength elements (HFSE) marked by Nb, Ta, Ti, and P (Fig. 9b). The samples have high Sr/Y ratios (49 to 61), although they also show elevated Y (27.68–33.42 ppm) and Yb (2.91–3.85 ppm) concentrations (Table 8). Transition element concentrations are very low with Cr from 12.12 to 30.79 ppm and Co from 14.35 to 30.89 ppm. Cu concentrations range from 9.23 to 39.00 ppm (except one at 109.86 ppm).

5.6. Sr-Nd-Pb isotopic composition of the granodiorite

The analyzed results of whole-rock Sr-Nd and Pb isotopic compositions of the Andagul granodiorite are presented in Table 9. The initial Sr isotopic ratios ($^{87}Sr/^{86}Sr)_i$ and $\epsilon_{Nd}(t)$ values are recalculated at the age of 307 Ma (mean zircon U-Pb ages). The Andagul granodiorite are characterized by relatively homogenous initial ($^{87}Sr/^{86}Sr)_i$ values from 0.7049 to 0.7059, and $\epsilon_{Nd}(t)$ values varying from +2.1 to +4.3 (Fig. 10a), with corresponding two-stage depleted-mantle Nd model ages (T_{2DM}) ranging from 728 Ma to 907 Ma (Table 9). Both ($^{87}Sr/^{86}Sr)_i$ and $\epsilon_{Nd}(t)$ values show no considerable variation with SiO_2 contents, which allows us to preclude considerable contamination from the upper crust during magma ascending.

Their whole-rock Pb isotopic compositions are characterized by high radiogenic Pb isotopic compositions with the present-day isotopic ratios varying from 18.946 to 19.022 for $^{206}Pb/^{204}Pb$, from 15.595 to 15.669 for $^{207}Pb/^{204}Pb$ and from 38.804 to 38.905 for $^{208}Pb/^{204}Pb$, respectively (Table 9). The initial Pb isotopic isotopic ratios were calculated at 307 Ma using the whole-rock Pb isotopic ratios and whole-rock U, Th and Pb contents (Table 8). The calculated initial Pb isotopic ratios are ($^{206}Pb/^{204}Pb)_t$ = 17.76 to 18.51, ($^{207}Pb/^{204}Pb)_t$ = 15.56 to 15.62, and ($^{208}Pb/^{204}Pb)_t$ = 37.89 to 38.33 (Table 9). They are presented in plots of $^{207}Pb/^{204}Pb$ against $^{206}Pb/^{204}Pb$ (Fig. 11a) and $^{208}Pb/^{204}Pb$ against $^{206}Pb/^{204}Pb$ (Fig. 11b) with references to the average growth curve of Zartman and Doe (1981), together with data from different terranes and intrusions (Chiaradia et al., 2006).

Table 8

Major (in wt%), trace and rare earth element (in ppm) compositions of the Andagul granodiorite.

Sample NO.	13Un-16	13Un-17	13Un-18	13Un-20	13Un-21	13Un-22	13Un-68	13Un-69	13Un-70	13Un-71	13Un-72	13Un-73	13Un-74
Major oxides (wt%)													
SiO_2	63.35	63.71	65.04	63.93	63.05	63.69	61.89	61.74	63.38	61.98	61.07	62.79	64.22
Al_2O_3	16.81	16.83	16.62	16.64	16.69	16.45	16.92	16.69	17.01	16.97	17.19	17.03	16.1
CaO	4.9	4.79	4.41	4.71	4.78	4.84	5.41	5.02	5.39	5.13	5.2	5.45	4.71
Fe_2O_3	0.53	0.16	0.83	1	0.71	0.84	0.45	1.26	0.31	1.2	0.42	0.06	1.39
FeO	3.27	3.77	2.8	3.05	3.16	3.13	4.17	4.06	3.84	3.63	4.6	4.38	3.81
K_2O	2.61	2.53	2.8	2.55	2.5	2.46	2.21	2.24	1.71	2.29	2.27	1.70	1.66
MgO	1.65	1.61	1.44	1.65	1.65	1.68	2.21	2.28	1.98	2.21	2.33	2.07	1.89
MnO	0.07	0.08	0.08	0.09	0.07	0.08	0.11	0.13	0.1	0.12	0.12	0.11	0.15
Na_2O	3.91	3.94	3.86	3.86	4.04	3.92	3.85	3.77	3.88	3.82	3.86	3.87	3.62
P_2O_5	0.19	0.19	0.18	0.19	0.17	0.18	0.19	0.19	0.18	0.19	0.19	0.18	0.17
TiO_2	0.53	0.52	0.48	0.51	0.49	0.49	0.54	0.56	0.53	0.55	0.57	0.55	0.5
LOI	1.29	0.93	1	0.82	2.66	1.27	1.2	1.14	1	1.04	1.19	0.84	0.94
Total	99.11	99.06	99.54	99	99.97	99.03	99.15	99.08	99.31	99.13	99.01	99.03	99.16
TFe_2O_3	4.16	4.35	3.94	4.39	4.22	4.32	5.08	5.77	4.58	5.23	5.53	4.93	5.62
Mg#	48	43	48	49	48	49	49	50	48	52	48	46	47
A/CNK	0.93	0.94	0.96	0.94	0.92	0.92	0.91	0.94	0.94	0.94	0.94	0.94	0.99
A/NK	1.82	1.83	1.77	1.83	1.78	1.81	1.94	1.93	2.07	1.94	1.95	2.07	2.08
Trace elements (ppm)													
Li*	23.06	19.91	28.51	25.35	18.33	17.23	49.80	51.45	45.49	49.92	48.85	45.62	47.94
Be*	3.86	3.38	3.31	3.29	3.36	3.33	4.03	4.15	3.44	4.00	3.60	3.51	4.64
Sc	17.85	15.35	13.39	15.57	15.22	17.06	23.23	22.22	22.36	21.68	23.80	21.90	21.33
Cu*	109.86	17.86	13.03	9.23	26.52	30.96	12.98	39.00	14.48	19.09	10.24	10.18	20.57
Zn*	78.45	99.93	106.27	123.65	64.50	72.67	102.52	119.61	103.31	115.24	108.41	106.96	119.97
Ga	44.71	42.72	42.90	41.72	41.26	41.42	42.67	42.93	41.50	43.12	43.37	42.08	41.08
Tl*	0.72	0.69	0.76	0.71	0.58	0.51	0.44	0.49	0.49	0.49	0.51	0.49	0.54
Bi*	0.42	0.11	0.15	0.17	0.29	0.13	0.03	0.04	0.13	0.03	0.10	0.10	0.05
Cs	8.84	7.84	7.66	7.55	8.96	6.97	10.10	10.94	11.26	10.92	11.77	11.57	13.09
Rb*	172.23	163.32	162.23	160.94	173.89	163.31	171.97	169.40	113.68	172.74	121.79	117.49	131.74
Ba*	3156.80	3149.02	3561.20	3025.54	2868.62	2776.06	3082.33	3091.86	2717.45	3281.29	2724.23	2692.09	2277.30
Th	22.38	22.21	18.95	18.76	19.41	18.60	18.11	14.53	21.48	17.49	22.08	22.79	20.16
U	8.13	4.54	5.09	5.60	5.51	5.90	7.05	5.12	11.29	7.21	8.67	8.09	8.94
Ta*	2.24	2.30	2.89	2.17	1.81	1.90	1.69	1.61	2.07	1.64	2.14	2.12	1.86
Nb	29.38	29.23	33.17	28.39	24.70	25.81	23.95	25.03	25.61	24.03	25.94	25.07	21.62
Sr	1542.61	1688.16	1725.75	1644.57	1632.79	1621.92	1897.35	1926.83	1788.50	1974.02	1823.66	1757.54	1630.88
Zr	313.42	334.72	316.92	301.38	291.39	285.20	305.33	296.32	267.91	290.26	299.18	282.14	254.91
Hf	8.67	9.33	8.75	8.32		7.73	8.15	7.78	7.44	7.69	8.25	7.77	7.16
Pb	34.30	29.49	35.12	32.96	21.79	23.16	22.75	25.31	27.92	25.00	28.43	26.24	25.06
V*	170.25	152.40	130.55	143.56	149.19	149.44	196.70	206.77	190.98	201.72	202.71	194.82	177.23
Cr*	15.89	12.12	15.14	12.23	18.27	16.75	21.71	21.95	22.81	28.61	30.79	23.47	18.27
Co	18.82	16.71	14.35	15.88	16.50	16.52	27.47	30.89	22.37	28.52	24.73	24.01	28.74
Ni*	20.46	11.59	12.87	13.41	26.19	65.29	31.47	33.25	25.34	46.09	13.15	16.35	24.92
La	62.97	68.87	66.13	65.48	66.03	33.23	61.56	54.19	60.94	61.26	62.89	61.40	57.40
Ce	117.70	124.37	120.17	116.67	117.89	113.74	108.62	101.23	106.84	108.39	112.55	109.60	93.83
Pr	13.07	14.38	15.21	13.82	13.47	13.07	12.86	12.42	12.28	12.88	13.17	12.90	10.76
Nd	49.83	53.82	58.68	51.61	49.66	49.13	49.37	47.96	46.27	49.11	49.48	48.63	39.64
Sm	9.02	9.02	10.31	8.81	8.20	8.56	8.75	8.83	8.09	8.72	8.81	8.50	6.92
Eu	2.40	2.30	2.49	2.27	2.16	2.19	2.26	2.20	2.20	2.28	2.29	2.21	1.87
Gd	7.89	7.94	8.64	7.65	7.21	7.48	7.76	7.70	7.22	7.76	7.90	7.62	6.31
Tb	1.15	1.10	1.20	1.06	0.99	1.04	1.13	1.12	1.05	1.13	1.14	1.11	0.93
Dy	6.03	5.77	6.09	5.40	5.24	5.60	6.19	6.11	5.85	6.14	6.19	6.08	5.09
Ho	1.18	1.14	1.18	1.02	1.01	1.11	1.31	1.26	1.24	1.28	1.30	1.26	1.06
Er	3.21	3.08	3.15	2.81	2.85	3.01	3.57	3.42	3.42	3.48	3.61	3.46	3.06
Tm	0.50	0.48	0.47	0.44	0.45	0.47	0.55	0.54	0.55	0.55	0.57	0.56	0.50
Yb	3.31	3.11	3.04	2.91	2.95	3.06	3.60	3.51	3.65	3.52	3.85	3.81	3.36
Lu	0.50	0.48	0.47	0.45	0.46	0.48	0.56	0.55	0.58	0.55	0.61	0.60	0.54
Y	31.60	30.34	30.93	28.49	27.68	29.64	33.42	32.54	31.88	32.48	34.38	32.83	29.08
Total REE	278.76	295.86	297.23	280.41	278.58	270.97	268.09	251.05	260.17	267.05	274.37	267.73	231.25
Eu/Eu*	0.85	0.81	0.79	0.83	0.84	0.82	0.82	0.80	0.86	0.83	0.82	0.82	0.85
(La/Yb)$_N$	13.66	15.91	15.60	16.14	16.06	14.55	12.27	11.06	11.98	12.47	11.70	11.55	12.25
(Dy/Yb)$_N$	1.22	1.24	1.34	1.24	1.19	1.23	1.15	1.16	1.07	1.17	1.08	1.07	1.01
(Gd/Yb)$_N$	1.97	2.12	2.35	2.17	2.02	2.02	1.78	1.81	1.64	1.82	1.70	1.65	1.55
T$_{Zr}$ (°C)	816	825	825	816	810	808	808	810	804	808	809	807	809

Note: Eu/Eu* = 2*EuN /(SmN + GdN) using concentrations normalized to chondrite.

6. Discussion

6.1. Petrogenesis of the Andagul intrusion

The mineralogical and geochemical characteristics of the Andagul intrusion, as described above, in particular the development of abundant plagioclase (ca. 55 vol%) and hydrous minerals (amphibole, biotite; ca. 15 vol%) (Fig. 4), medium contents of alkalis (Fig. 8a and b) and magnesian-rich geochemical nature (Fig. 8d), are significantly different from the widely distributed early Permian A-type granites (Rapakivi) in the Tian Shan (Konopelko et al., 2007; Solomovich, 2007; Solomovich and Trifonov, 2014). Lacking of diagnostic peraluminous

Table 9
Whole rock Rb-Sr, Sm-Nd and Pb isotopic data for the Andagul granodiorite.

Sample	13Un-16	13Un-17	13Un-18	13Un-19	13Un-20	13Un-21	13Un-22	13Un-68	13Un-69	13Un-70	13Un-71	13Un-72	13Un-73	13Un-74
$^{87}Rb/^{86}Sr$	0.327	0.284	0.276	0.287	0.312	0.295	0.266	0.258	0.186	0.257	0.196	0.196	0.237	0.258
$^{87}Sr/^{86}Sr$	0.706370	0.706354	0.706319	0.706308	0.706313	0.706342	0.706326	0.706712	0.706204	0.706741	0.706723	0.706734	0.706758	0.706534
1σ	9	8	7	6	9	8	7	9	8	9	8	7	9	8
$^{87}Sr/^{86}Sr$ (i)	0.7049	0.7051	0.7051	0.7051	0.7049	0.7051	0.7052	0.7056	0.7054	0.7056	0.7059	0.7059	0.7057	0.7054
$^{147}Sm/^{144}Nd$	0.1101	0.1018	0.1068	0.1064	0.1038	0.1004	0.1060	0.1078	0.1119	0.1063	0.1079	0.1082	0.1062	0.1061
$^{143}Nd/^{144}Nd$	0.512623	0.512648	0.512621	0.512618	0.512634	0.512625	0.512619	0.512571	0.512586	0.512559	0.512579	0.512658	0.512568	0.512671
1σ	7	9	8	9	7	10	8	9	7	6	8	9	7	8
$^{143}Nd/^{144}Nd(i)$	0.51240	0.51244	0.51241	0.51240	0.51243	0.51242	0.51241	0.51235	0.51236	0.51235	0.51236	0.51244	0.51235	0.51246
$\varepsilon_{Nd}(0)$	-0.1	0.4	-0.2	-0.2	0.1	-0.1	-0.2	-1.2	-0.9	-1.4	-1.0	0.5	-1.2	0.8
$\varepsilon_{Nd}(i)$	3.2	4.0	3.3	3.3	3.7	3.7	3.3	2.3	2.4	2.1	2.5	4.0	2.3	4.3
T_{DM}	778	687	757	758	718	709	754	836	847	842	825	714	828	681
T_{2DM}	817	751	810	813	779	783	810	892	882	907	880	755	892	728
U(ppm)	3.85	3.95	2.36	2.64	2.71	2.62	2.85	3.27	2.40	5.39	3.43	1.13	3.98	4.31
Th(ppm)	10.98	11.34	10.89	9.53	8.94	9.13	9.14	8.56	7.01	9.25	8.24	3.01	10.86	9.01
Pb(ppm)	15.87	16.38	15.03	16.84	15.69	9.87	10.85	13.26	14.27	13.82	13.53	6.00	14.55	14.19
$^{206}Pb/^{204}Pb$	18.961	18.957	19.003	19.011	18.965	19.022	18.968	18.992	18.975	18.984	18.981	18.946	18.997	18.985
1σ	24	32	25	26	25	27	25	28	23	26	25	31	30	28
$^{207}Pb/^{204}Pb$	15.631	15.595	15.638	15.641	15.597	15.649	15.632	15.658	15.643	15.669	15.656	15.652	15.659	15.663
1σ	26	23	26	29	32	27	25	27	27	21	26	28	33	30
$^{208}Pb/^{204}Pb$	38.815	38.802	38.819	38.823	38.804	38.835	38.819	38.862	38.831	38.859	38.854	38.842	38.846	38.905
1σ	26	23	31	26	32	28	24	30	27	28	25	27	27	31
$(^{206}Pb/^{204}Pb)_i$	18.20	18.20	18.51	18.52	18.42	18.19	18.14	18.22	18.45	17.76	18.18	18.36	18.14	18.03
$(^{207}Pb/^{204}Pb)_i$	15.59	15.56	15.61	15.62	15.57	15.61	15.59	15.62	15.62	15.60	15.61	15.62	15.61	15.61
$(^{208}Pb/^{204}Pb)_i$	38.11	38.10	38.08	38.25	38.22	37.89	37.96	38.20	38.33	38.18	38.23	38.33	38.09	38.26

minerals such as muscovite, cordierite, and garnet (Fig. 4) and relatively low A/CNK ratios (less than 1.0; Fig. 8c) exclude to the Andagul intrusion from the series S-type granites of supracrustal origin (Barbarin, 1999). The Andagul granodiorite is best classified as calc-alkaline I-type series based on their mineralogical and geochemical characteristics.

Petrogenetic models of calc-alkaline I-type granitoids are diverse, including (1) crustal fractionation crystallization or assimilation-fractional crystallization (AFC) process of mantle-derived magma (Fowler et al., 2008); (2) partial melting of a subducted oceanic slab (Martin et al., 2005; Tarney and Jones, 1994); (3) partial melting of enriched lithospheric mantle that had been metasomatized by subduction-related fluids and/or melts (Peng et al., 2013); and (4) Partial melting of an ancient or juvenile basaltic lower crust (Hou et al., 2013).

In order to produce the I-type granitoids through fractionation of mantle derived magmas, extreme fractionation would be required and large amounts of basaltic magma (one order of magnitude more than the felsic magma) would have been produced. The lacking of coexisting basaltic rocks in the Kassan region suggests that such a mechanism was unlikely to be responsible for the generation of the Andagul granitic magma. The consistent composition of the Andagul granodiorite and absence of gabbro-diorite-granodiorite suites in the Kassan region also argues against the fractionation of basaltic magma as a mechanism for the formation of the intrusion. On the plots of Ta/Sm vs. Ta, the Andagul granodiorite samples exhibit a well-defined linear trend, suggesting that the partial melting process rather than magmatic fractionation plays an important role in the granitic magma generation (Fig. 8j).

The Na_2O domination over K_2O, elevated Sr (> 300 ppm), relatively high Sr/Y ratios (average of 55.94) and pronounced REE fractionation of the Andagul granodiorite are reminiscent of adakite rocks (Defant and Drummond, 1990). However, the high Y (> 27 ppm) and Yb (> 2.9 ppm) contents together with low Cr, Co and Ni concentrations (Table 8) are evidently different from typical adakitic rocks of slab-melting origin (Defant and Drummond, 1990). In terms of their major element composition, they follow a distinctive calc-alkali enrichment trend (Fig. 8e) (Fowler et al., 2008), unlike the generally trondhjemitic adakites (Martin et al., 2005) Thereafter, the possibility of the partial melting of a subducted oceanic slab is also ruled out.

The enrichment of LILE and marked depletion of Nb, Ta, Ti and P of the Andagul granodiorite (Fig. 9b) has been recognized as a typical fingerprint of subduction processes. Moreover, the Andagul granodiorite shows similar geochemical patterns with the Carboniferous subduction-related granites from the Almalyk region (Fig. 9b), suggesting a common source that was metasomatized by slab-derived fluids or melts during subduction of the Turkestan Ocean (Cheng et al., 2017; Dolgopolova et al., 2017). However, it seems not necessary to conclude that these magmatic rocks were produced in a subduction setting since subduction components may be inherited from the previous metasomatized subcontinental mantle lithosphere (SCML) or newly underplated lower crust (Dolgopolova et al., 2017). The positive $\varepsilon_{Hf}(t)$ values ($+2.29$ to $+4.80$) and $\varepsilon_{Nd}(t)$ ($+2.1$ to $+4.3$) of the Andagul intrusion, which are close to depleted mantle values (Fig. 7), rule out the possibility that the magmas were derived directly from enriched SCLM, which usually gives a range of $\varepsilon_{Hf}(t)$ and $\varepsilon_{Nd}(t)$ values from -12 to -36 and -7.4 to -15.4, respectively (Hou et al., 2013). Therefore, the most likely origin of the Andagul granitic magma was generated through partial melting of newly underplated lower crust, as further elaborated below.

The relatively low positive $\varepsilon_{Nd}(t)$ and $\varepsilon_{Hf}(t)$ values of the Andagul granodiorite may indicate that the source rocks are from a weakly depleted mantle, or that the source rocks are from a depleted mantle but there are also contributions from crustal materials. The presence of inherited zircon, relatively high $(^{87}Sr/^{86}Sr)_i$ ratios and Proterozoic model ages ($T_{2DM}(Hf) = 1026$ to 1175 Ma, $T_{2DM}(Nd) = 728$ to 907 Ma) suggest such a scenario as anatexis of ancient basement or analogous
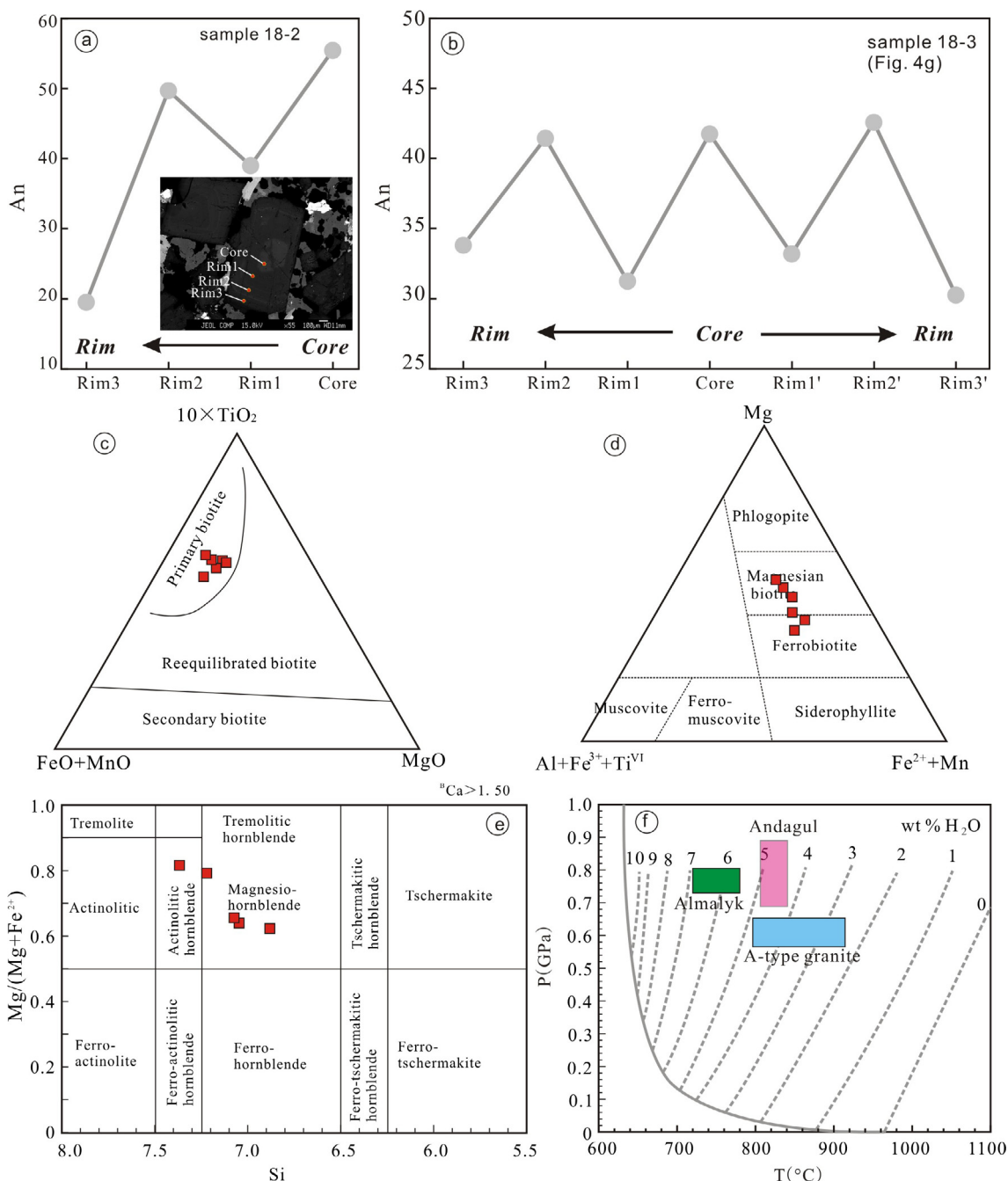
Fig. 5. Electron microprobe profiles (a, b) for plagioclase showing oscillatory zoning of An (Anorthite) component from core to rim; c. discrimination diagram for biotite (Bt) after Nachit et al. (2005); d. Biotite compositional classification from the Andagul intrusion in the ternary Mg-(Fe^{2+} + Mn)-(^{VI}Al + Fe^{3+} + Ti) diagram; e. Si (a.p.f.u.) versus Mg/(Mg + Fe^{2+}) diagrams for calcic-amphiboles after Leake et al. (1997); f. Estimate of water contents (wt% H_2O) in the initial granitoid melts for granitoid intrusions from the Andagul, Almalyk region and A-type granite in STS, based on the model of Holtz et al. (2001). The subduction-related granites in Almalyk region and the A-type granites in the STS are recalculated from the data of Cheng et al. (2017), Konopelko et al. (2007, 2009) and Solomovich (2007).

continental rocks may have been involved in the formation of the Andagul granodiorite magma. The Pb isotopic compositions of the Andagul granodiorite are consistent (Table 9) and plot away from the upper crust schists and slightly above the orogen curve (Fig. 11) (Zartman and Doe, 1981), reflecting a homogeneous reservoir as is a typical of the continental arc environment where mantle-derived magmas interact with continental crust rocks (Chiaradia et al., 2006). A binary modeling with Sr and Nd isotopes between depleted mantle and ancient basement crust, represented by Bayingou ophiolite and Neo-proterozoic granitoid gneiss, respectively, reveals that only ca. 5–10% of basement rocks may have been involved in the formation of the

Andagul granodiorite magma (Fig. 10b). Thus, the dominant (> 90%) source material for the Andagul magma may still be derived from the mantle (Fig. 10b).

The geochemical characteristics of the Andagul intrusion as discussed above resemble to granitic intrusions derived from newly un-derplated basaltic lower crust or juvenile lower crust as reported else-where (Hou et al., 2013; Petford and Atherton, 1996). The absence of marked Eu anomalies and high Sr contents (Fig. 9b) may reflect that plagioclase removal played an insignificant role in the genesis of the magma, while the highly fractionated LREE to HREE and typical flat to concave-up MREE to HREE patterns (Fig. 9a) suggest the involvement
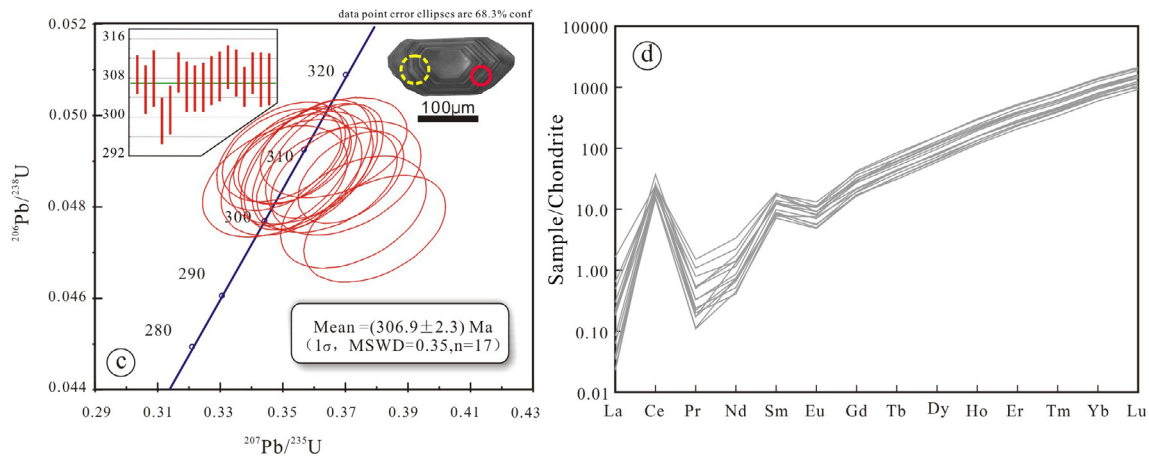
Fig. 6. U-Pb concordia diagrams (a) and chondrite-normalized trace element diagram (b) of zircon samples with LA-ICPMS. The red circle and yellow broken circle on cathodoluminescence image of representative zircon show U-Pb and Lu-Hf analytical spots, respectively. (For interpretation of the references to color in this figure legend, the reader is referred to the web version of this article.)

of garnet and amphibole as cumulates in the parental magma or residual phases in the source rocks (Martin et al., 2005; Richards, 2011a). The breakdown of amphibole may have also played an important role in dehydration melting, which may have supplied initial water to generate melt at the initial stage of melting (Rapp and Watson, 1995).

Melting of the basaltic lower crust requires an additional heat from the mantle, which may be provided by asthenospheric upwelling following thinning of the lithospheric mantle (Petford and Atherton, 1996). The calculated Zr saturation temperature (T_{Zr}) of the Andagul granodiorite (804 °C to 825 °C, to be discussed in more detail below), which may represent the maximum estimation of magma temperature due to the presence of inherit zircon (Fu et al., 2008), is consistent with such a requirement of heat input from the deep mantle. Additionally, the $Mg^{\#}$ values (43–52), which are higher than those of pristine experimental melts of metabasalts and eclogite lower than 40 regardless of melting degrees (Rapp and Watson, 1995), also imply the involvement of mantle components. The presence of mafic enclaves (Fig. 4c), acicular apatite (Fig. 4h) and disequilibrium textures such as oscillatory plagioclases (Figs. 4g–h, 5a–b) and oscillatory titanite (Fig. 4i) further suggest an injection of mantle-derived melt (as potential supply for volatiles and metals) and heat.

The emplacement age of the Andagul granodiorite (299 to 310 Ma) (Fig. 6) was right after the peak metamorphism (ca. 317 Ma) and subsequent rapid exhumation time (ca. 312 Ma) of the high-pressure

Kassan Metamorphism Complex (Mühlberg et al., 2016), and therefore indicate a post-collisional setting. Besides, it bridges the carboniferous arc-related magmatism (330–310 Ma) and the Early Permian post-collisional magmatism (295–270 Ma), the latter being characterized by diverse types of voluminous magmatism across different terranes and commonly interpreted as resulting from slab break-off or delamination (Konopelko et al., 2018; Solomovich and Trifonov, 2002). Thus, the Andagul granodiorite is plausibly associated with a tectonic transition regime during which the stress field transforms from regional compression into post-collisional extension. Partial melting of the juvenile lower crust with arc magma signatures and a small proportion of basement rocks was triggered by episodic mantle upwelling.

6.2. Physico-chemical conditions of magma crystallization

The geochemical data documented above are further used to estimate the temperature and pressure conditions of magma crystallization of the Andagul intrusion. The water and oxygen fugacity of the magma are also discussed.

6.2.1. Temperature
Zircon in a cooling magma grows over a range of temperature that begins at zircon saturation and culminates at the solidus and there is an interval of some 100° to 200 °C between the solidus and the liquidus for
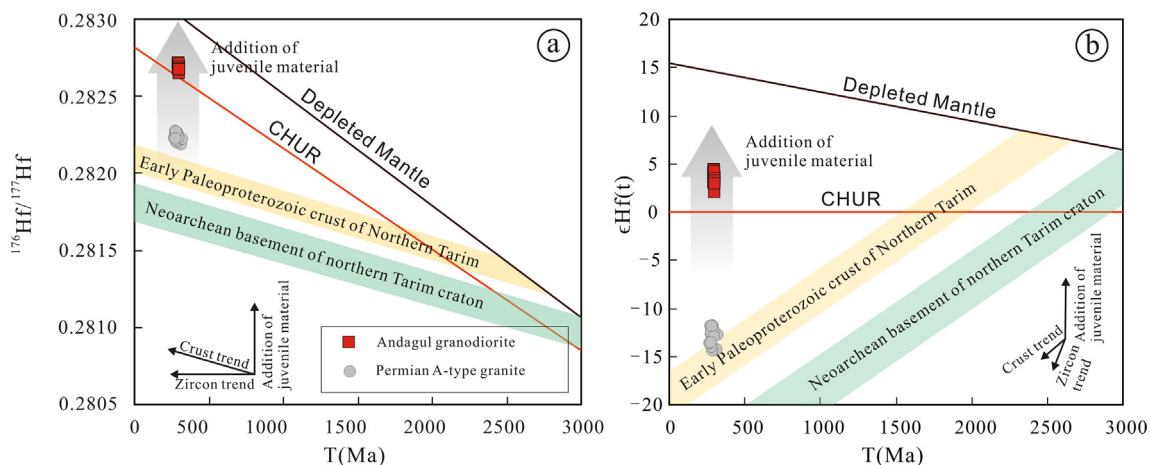
Fig. 7. Hf isotope data of the dated zircons for the Andagul granodiorite samples. (a) Initial $^{176}Hf/^{177}Hf$ vs. age diagram and (b) $\varepsilon_{Hf}(t)$ vs. age diagram. Evolution lines of the early Paleoproterozoic crust and Neoarchean basement of the northern Tarim are cited from Long et al. (2012). The data of Permian A-type granite are from Konopelko et al. (2013).
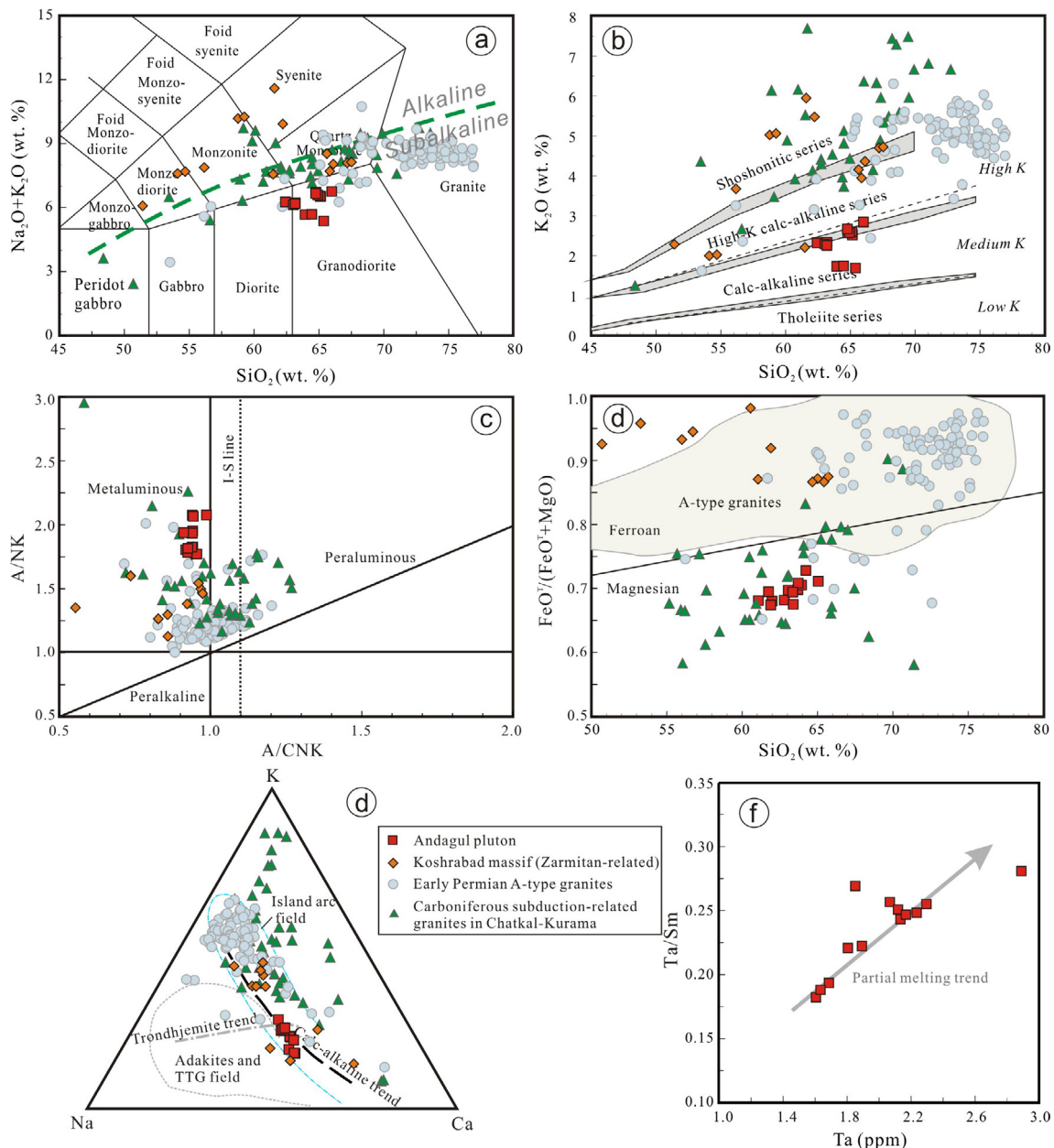
Fig. 8. Principal geochemical classification diagrams for the Andagul granodiorite in the Kassan region: (a) Total alkali vs. silica (TAS) diagram (Middlemost, 1994); (b) K₂O vs. SiO₂ diagram; (c) A/NK vs. A/CNK plot; A/CNK = Al₂O₃/(CaO + Na₂O + K₂O) molar, A/NK = Al₂O₃/(Na₂O + K₂O) molar; (d) FeOᵀ/(FeOᵀ + MgO) vs. SiO₂, wt.% with a field for A-type granites of the world; (e) Na-K-Ca plot (Tarney and Jones, 1994); and (f) Ta/Sm vs. Ta plot. Data sources: The data of Permian Koshrabad massif that host Zarmitan IRG deposit in the STS followed Konopelko et al. (2011); A-type (Rapakivi) granites in Kyrgyz South Tian Shan are compiled from Konopelko et al. (2007, 2009), Solomovich (2007) and Solomovich and Trifonov (2002); The Late Carboniferous subduction-related granites in Almalyk are from Cheng et al. (2017).

most magmatic compositions (Fu et al., 2008). The zircon saturation temperatures are calculated assuming that the whole rock data reflect magma compositions following the method of Watson and Harrison (1983). Using this methods, the Andagul granodiorite zircon data yielded temperatures of 804° to 825 °C with an average of 814 °C (Table 8).

The Ti-in-zircon thermometer is calculated following the method of (Ferry and Watson, 2007) by setting the activity of SiO₂ to 1 considering the widely presence of primary magmatic quartz. The activities of TiO₂ is conservatively estimated to be 0.70 considering the presence of titanite and magnetite (Fu et al., 2008). The calculated temperatures are mostly in the range from 586° to 763 °C with an average of 683 °C (Table 6).

The Ti-in-biotite thermometer is also employed to estimate crystallization temperature of biotite from the Andagul intrusion (Henry, 2005). The calculated temperatures range from 710° to 748 °C with an average of 736 °C (Table 2).

Amphibole thermo-barometric equations of Ridolfi et al. (2010) were obtained with different analytical and experimental approaches. The temperature is correlated with silicon index (R₂) and is a little affected by P and Al₂O₃ variation (Ridolfi et al., 2010). Temperatures calculated with this method range from 738° to 810 °C with an average of 772 °C (Table 3).

The Zr saturation temperature (average 814 °C) may represent the minimum melting temperature of the magma considering the absence of inherited core (Fig. 6a). The crystallization temperature of zircon
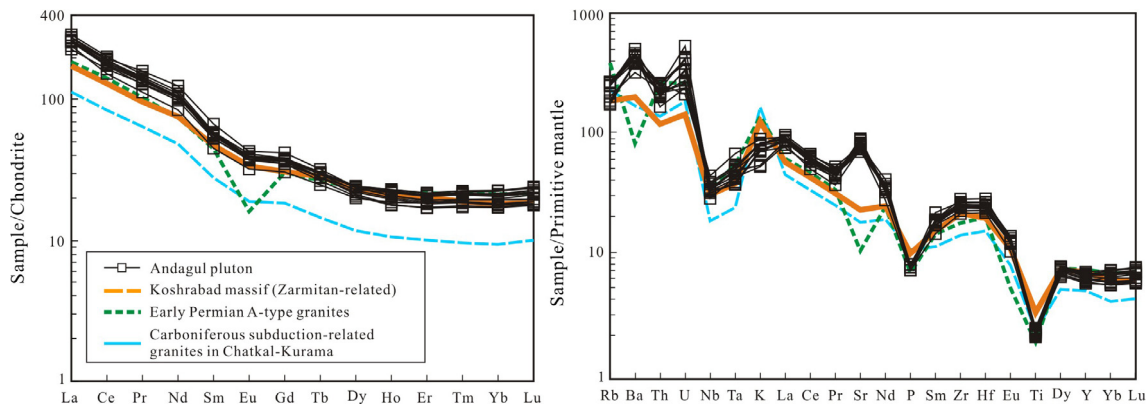
Fig. 9. Whole rock rare earth element spider diagram (a) and trace element distribution pattern (b). Data of the Zarmitan gold related Koshrabad massif, Early Permian A-type granites and Carboniferous subduction-related granites in Almalyk are compiled from the same data source as in Fig. 8.

should be lower than this temperature. Based on the petrographic observations that biotite and zircon occurs with plagioclase and quartz or in the matrix, and amphibole occurs as large euhedral crystals or as large phenocrysts (Fig. 4d and e), it is inferred that amphibole crystallized earlier than biotite and zircon, which appears to be consistent with the calculated crystallization temperatures of the different minerals. The relatively low temperatures estimated by the Ti-in-zircon thermometer may be related to the hydrous nature of the parental magma (> 4 wt% H_2O, see 6.3.3) (Fu et al., 2008). Therefore, the calculated average temperatures of 784 °C, 736 °C and 683 °C for amphibole, biotite and zircon, respectively, could plausibly record the crystallization history of the magma.

6.2.2. Pressure

The Al-in-amphibole geobarometry (Anderson and Smith, 1995) has been widely used to estimate the pressures of crystallization of igneous hornblende that is associated with the assemblage of quartz, plagioclase, orthoclase, biotite, amphibole, titanite, and magnetite, as is the case for the Andagul intrusion. This barometry is suitable for hornblende having $0.4 < Fe^{tot}/(Fe^{tot} + Mg)$ less than 0.65 and $0.2 < Fe^{3+}/(Fe^{3+} + Fe^{2+})$, where Mg and Fe are calculated on the basis of 13 cations. The estimated pressures according to this geobarometry range from 1.22 to 1.25 kbar, corresponding to depths of 4.5 to 4.6 km (assuming an average density of 2.7 g/cm^3 for the upper crust).

Pressure estimates were also made utilizing the thermo-barometric equations of Ridolfi et al. (2010) that originally applied to volcanic and experimental amphiboles and then successfully extended to the plutonic amphiboles (Turnbull et al., 2010). The prerequisite to using this barometer is a calc-alkaline magma-derived amphibole that has a composition of $Al^{\#}$ (Al^{VI}/Al^{tot}) ≤ 0.21 and $Mg^{2+}/$ ($Fe^{2+} + Mg^{2+}$) > 0.5, which suits the Andagul intrusion. The calculated pressures range from 0.61 to 1.36 kbar, and the corresponding depths range from 2.3 to 5.0 km.

6.2.3. Water content

Water content in magma plays a key role in water saturation and exsolution of magmatic intrusions, and thus is the sine qua non of magmatic-hydrothermal ore-forming systems (Richards, 2011a). The order of crystallization of minerals such as hornblende, feldspar, and magnetite can provide evidence of the initial water content of the melts. The Andagul granodiorite is featured with strikingly high Sr and Ba contents (Fig. 9b), absence of marked Eu anomalies (Fig. 9a) and low Y concentrations. These characteristics suggest that little plagioclase fractionation (or restite) occurred early in the evolution of the magma, whereas hornblende was an important early crystallizing phase, which in turun suggest that the magmas of the Andagul granodiorite were relatively hydrous (> 4 wt% H_2O) and experienced fractional crystallization at relatively deep crustal levels (Richards, 2011a).

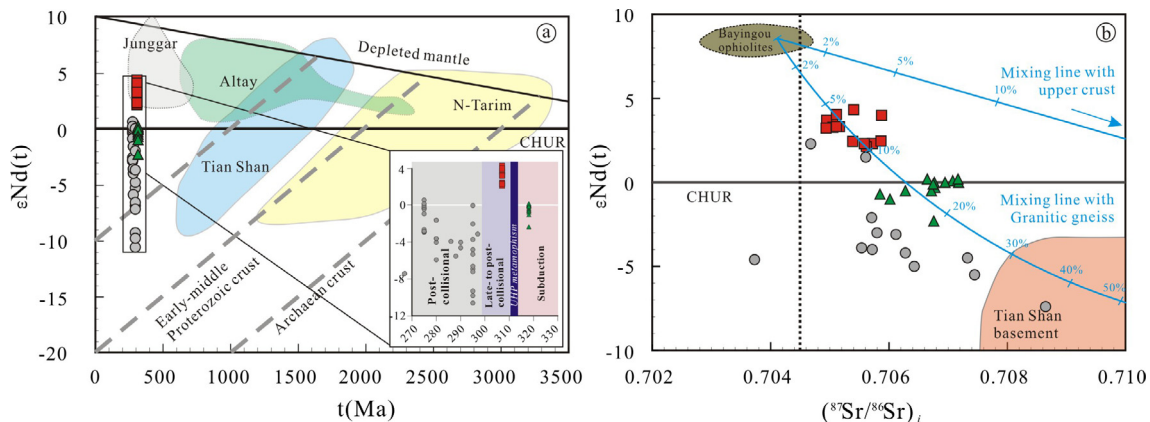The water solubility in felsic melts is a function of P, T, X, and water

Fig. 10. Diagrams of $\varepsilon_{Nd}(t)$ vs. t (a) and $\varepsilon_{Nd}(t)$ vs. ($^{87}Sr/^{86}Sr)_i$ (b) for the Andagul granodiorite. Fields of basement rock (amphibolites and granitic gneiss) of the Altay, Junggar and Tian Shan are after Long et al. (2011). The depleted mantle and lower crust mixing curves are constructed using the fowling end-member parameters: ① a basaltic lava sample of Bayingou ophiolite (011B75) from Xu et al. (2006): $\varepsilon_{Nd}(t)$ = 8.69, ($^{87}Sr/^{86}Sr)_i$ = 0.70410, Sr = 127 ppm, Nd = 10.7 ppm; ② a Neoproterozoic (ca. 707 Ma) granitoid genesis sample 966,006 from Chen et al. (2000) is recalculated to 307 Ma before modelling: $\varepsilon_{Nd}(t)$ = −10.4, ($^{87}Sr/^{86}Sr)_i$ = 0.71281, Sr = 251.2 ppm, Nd = 51.61 ppm; ③ upper continental crust (Taylor and Mclennan, 1985): $\varepsilon_{Nd}(t)$ = −10, ($^{87}Sr/^{86}Sr)_i$ = 0.72, Sr = 350 ppm, Nd = 26 ppm. Symbols are as in Fig. 8.
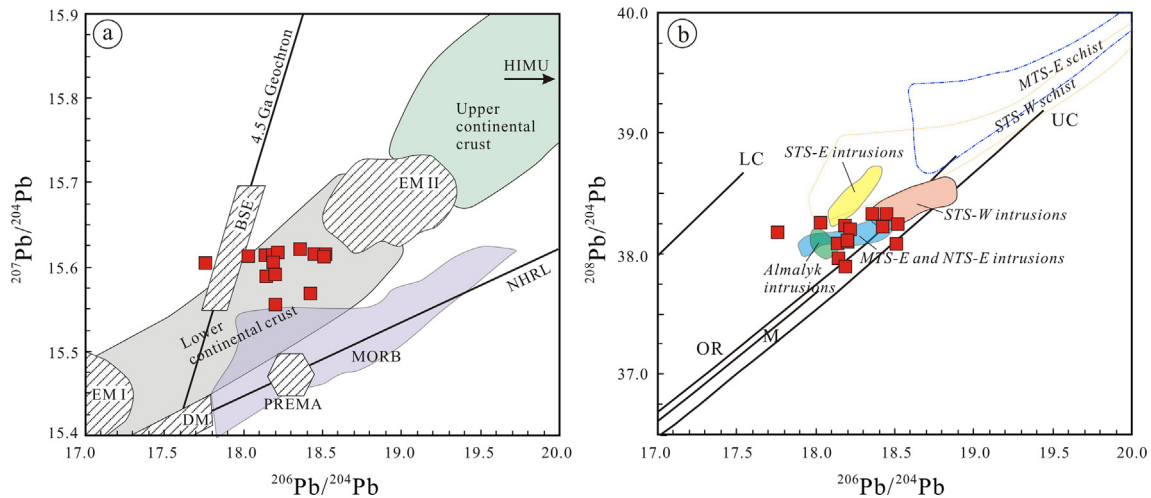
Fig. 11. $^{207}Pb/^{204}Pb$ vs $^{206}Pb/^{204}Pb$ and $^{208}Pb/^{204}Pb$ vs $^{206}Pb/^{204}Pb$ diagrams of the Andagul granodiorite. All the isotopic ratios were corrected to 307 Ma. Data of the different terranes and Almalyk intrusions are from Chiaradia et al. (2006). The upper crust (UC), lower crust (LC), orogen (OR) and mantle (M) evolution curves are from Zartman and Doe (1981). MTS-E: Middle Tian Shan east of the Talas-Fergana fault; NTS-E: North Tian Shan east of the Talas-Fergana fault; STS-E: South Tian Shan east of the Talas-Fergana fault; STS-W: South Tian Shan west of the Talas-Fergana fault.

activity, which can be estimated based on the experiment of (Holtz et al., 2001). Assuming that the Andagul granodiorite magma was originally derived from the deep lower crust and using the zircon saturation temperatures to represent the initial liquidus temperatures, the minimum water contents in the initial melts of the Andagul granodiorite approximately vary from ~4.0 to 5.5 wt% in the 0.6 GPa to 0.9 GPa range of temperature, which are higher than that in the A-type granite melts in STS (~2.5–5 wt%) and lower than arc magmas of the intrusions of the Almalyk complex (~5.5–7 wt%) (Fig. 5g). These estimated water contents are consistent with those estimated with another method based on the $Al^{\#}$ values of amphibole using the equation (3) in Ridolfi et al. (2010), which range from 4.0 to 5.2 wt% (Table 3) with an average of 4.6 wt%. The high water contents in the initial melt may be caused by the breakdown of amphibole in the lower crust during the dehydration melting, consistent with the mineral assemblage and phase diagram results in the preceding discussion (Richards, 2011a).

6.2.4. Oxygen fugacity

The oxygen fugacity of a granitic magma exerts major influence on metal enrichment in magmatic-hydrothermal systems (Hart et al., 2004). The Andagul granodiorite characterized by development of titanite, primary magnetite and rutile and absence of ilmenite, indicating a relatively oxidizing condition which is also reflected by the Ce valences in zircon as discussed below.

Ce anomaly in zircon has been widely used as a robust proxy for the oxygen fugacity of magmas (Ballard et al., 2002; Smythe and Brenan, 2016). The Ce^{4+}/Ce^{3+} ratios of melts were calculated from a lattice strain model (Ballard et al., 2002), and the oxygen fugacities were estimated using the calibration methods of Smythe and Brenan (2016), which depend on temperature, water content and composition of the melt. Using the temperature obtained from the Ti-in-zircon thermometer (Ferry and Watson, 2007) and the water content estimated from the $Al^{\#}$ composition of the amphibole (Ridolfi et al., 2010), the oxygen fugacities ($logfO_2$) estimated from the Ce anomaly of zircon from the Andagul granodiorite fall in a narrow range from -19.27 to -16.80 (Table 6), corresponding to $\Delta FMQ = -0.33 \sim +0.49$ (Fig. 12). These oxygen fugacities are lower than those typical of magmas associated with porphyry Cu-Au mineralization (higher than $\Delta FMQ +2$; (Sun et al., 2015) and are comparable with those associated with intrusion-related Au deposits worldwide (Yang et al., 2006).
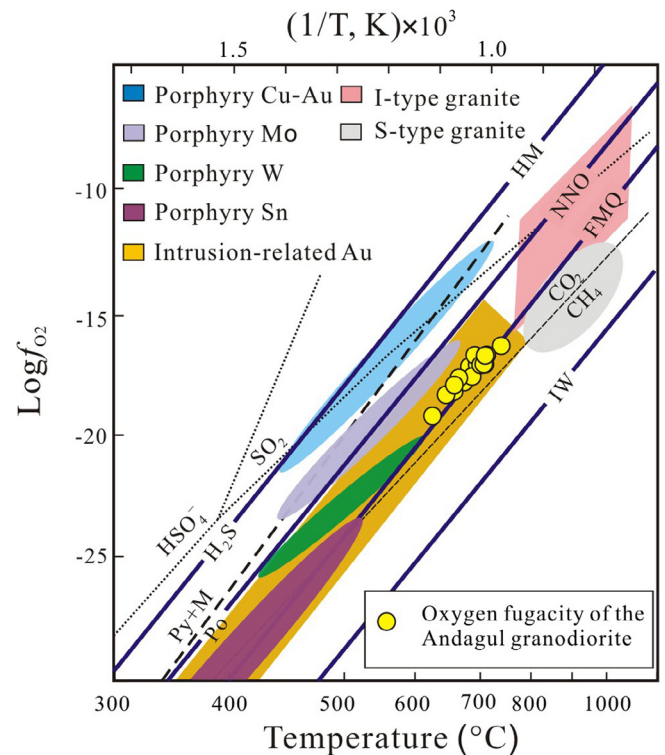

Fig. 12. Temperature vs oxygen fugacity diagram for the Andagul granodiorite. The thick lines show the conditions for the redox buffers HM (hematite and magnetite), NNO (NiO and Ni), FMQ (quartz, magnetite and fayalite) and IW (iron-wustite). Data of porphyry Cu-Au, porphyry Mo, porphyry Sn, porphyry W, intrusion-related gold deposits, I and S type granites are compiled by Yang et al. (2006).

6.3. Implication for Au mineralization

Many gold deposits in the Tian Shan are located within Late Paleozoic granitoid intrusions and their contact metamorphic aureoles (Abzalov, 2007; Kempe et al., 2016; Wall et al., 2004). Where radiometric dates have been obtained, mineralization is found to be broadly coincident with magmatism (Mao et al., 2004; Morelli et al., 2007; Yakubchuk et al., 2005). Furthermore, a number of recent geochemical
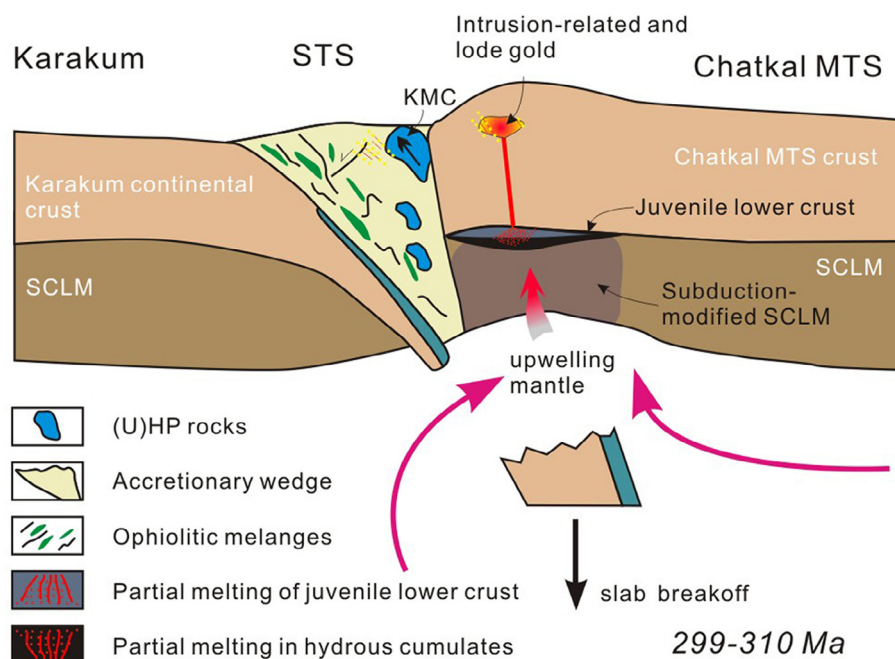
Fig. 13. Simplified cartoon showing the partial melting of the juvenile lower crust and hydrous sulfide cumulates leads to the formation of the Andagul granitoids and associated Au mineralization in a post-collisional setting. In the previous subduction stage, the upwelling of subduction metasomatized basaltic magma pondered in the boundary between SCLM and lower crust, where they underwent MASH processes, and lead to the formation of porphyry-related Cu-Au deposit (e.g. Almalyk region) with high oxygen fugacity state (Richards, 2009). Small amounts of sulfide (typically with high Au/Cu ratio) retained in cumulate zones and remelted with juvenile lower crust in the scenario of upwelling hot mantle probably due to tectonic stress transition. The resulting generated magma is characterized by high water content and slightly reduced redox state, optimum for the transport and enrichment of Au in melt.

and isotopic studies have led to mineralization models that implicate Late Paleozoic I-type granitoids as the source of metals and/or fluids for spatially associated gold deposits in the Tian Shan (Cole et al., 2000). As elaborated above, the concentric gradual change of metal associations and mineralization characteristics of gold deposits around the Andagul granodiorite intrusion in Kassan region (Fig. 1c) hint a possible genetic relationship between the mineralization and the intrusion. The fact that the zircon U-Pb age of the Andagul granodiorite (ca. 307 Ma) obtained in this study is nearly identical to the molybdenite Re-Os age (307.6 ± 1.5 Ma, our unpublished data) for the intrusion-hosted Unkurtash gold deposit strongly supports such a magmatic-hydrothermal mineralization model.

The Andagul granodiorite is inferred to have formed dominantly from partial melting of juvenile basaltic lower crust in juxtaposition with a precursor accretionary margin (Fig. 13), which may provide significant amount of Au inherited from the previous subduction-related magmatic systems (Hou et al., 2013; Richards, 2009; Richards, 2011b). A two stage melting model (Solomon, 1990) is introduced here to explain the Au-rich mineralization in the Kassan region, which postdates the porphyry Cu-Au mineralization in the nearby Almalyk region in the Chatkal-Kurama area. The lithosphere mantle and the juvenile lower continental crust were pregnant with metals from a long-lived subduction event of the Turkestan Ocean during the Paleozoic. Melting of the fertile SCLM and basaltic lower crust under oxidizing conditions during plate subductin leads to the formation of porphyry Cu-Au deposits in the Almalyk region (Fig. 12). Due to the different partition coefficients of Cu and Au in the sulfide phase relative to silicate melt, the magma could be enriched in Cu but depleted in Au when moderate amounts of sulfide are present relative to the volume of silicate melt ($R > 10^5$) (Richards, 2009; Richards, 2011b). Thus, the first-stage melting tends to generate Cu-Au deposits from the fertile source and leave a relatively Au-rich sulfide residual in cumulate zones due to density differences (Richards, 2009). Recent studies have suggested that the subduction fertilized garnet amphibolite or amphibolite lower continental crust could contain as much 6–16 ppb Au with high Au/Cu ratios (as much as 8×10^{-4}), thereby having the potential to generate significant Au-rich ore-forming systems after the subduction (Hou et al., 2017). Remobilization of this sulfide cumulate residual zone accompanying with the remelting of the fertilized juvenile lower crust due to thermal perturbation or mantle upwelling could provide a source of

metals (especially Au) for the intrusion-related gold deposits in post-collisional settings (Fig. 13). High initial water in the source rocks facilitates the remelting of the lower crust. Episodic injection of mantle component may provide additional volatile and metals for the mixed magma (Hattori and Keith, 2001).

Redox condition is a controlling factor for the development of intrusion-related gold systems (Blevin, 2004; Hart et al., 2004). Crystallization of magnetite in an oxidized melt, or pyrrhotite in a reduced melt, will sequester Au and have significant effects on the Au budget of a melt (Rowins, 2000; Yang et al., 2006). It has shown that the Au partition coefficients (Kd values) between mineral and melt for pyrrhotite and magnetite are similar (36 and 14, respectively), but they are several orders of magnitude smaller than for that for chalcopyrite (2×10^4) (Rowins, 2000). In order to retain Au within the melt, it is important that early crystallization of sulfides be suppressed and the sulfur remains undersaturated. Oxygen fugacities between NNO and FMQ are favorable for retaining Au in the melt; higher oxygen fugacities would favor Au partitioning into SO^{2-} bearing fluid phases while lower fO_2 would facilitate Au partitioning into early crystallizing sulfides (Blevin, 2004). In addition, experiments indicate that the volatile/melt partition coefficients of Au in a pyrrhotite saturated magma are as high as 200, while those for Cu is only 2 (Zajacz et al., 2012). Consequently, volatiles exsolving from mafic to intermediate melts will be important contributors to the Au and S but not Cu budget of Au-rich magmatic-hydrothermal ore deposits and relatively low fO_2 ($<$ NNO + 1) is likely to increase the Au/Cu ratios in hydrothermal deposits (Zajacz et al., 2012). The weakly oxidized or slightly reduced redox state near FMQ (ΔFMQ = $-0.33 \sim +0.49$) estimated from Ce anomaly for the Andagul granodiorite suggest that magnetite or sulfide would not crystallize substantially and therefore the redox conditions may be considered optimal for the retention of Au in the magma until volatile saturation occurs (Fig. 12).

7. Conclusions

The metal associations and zonation of gold deposits around the Andagul granodiorite intrusion in the Kassan region resembles typical magmatic-hydrothermal systems, suggesting that the gold mineralization is genetically related to the granitic intrusion.

Relatively low positive ε_{Nd}(t) values (+2.1 to +4.3), moderately

low ($^{87}Sr/^{86}Sr)_i$ ratios (0.7049 to 0.7059), relatively low initial Pb isotopic ratios (($^{206}Pb/^{204}Pb)_t$ = 17.76 to 18.51, ($^{207}Pb/^{204}Pb)_t$ = 15.56 to 15.62, and ($^{208}Pb/^{204}Pb)_t$ = 37.89 to 38.33), and juvenile $\varepsilon_{Hf}(t)$ (+2.29 to +4.80) signatures indicate that the magma of the Andagul intrusion was sourced from partial melting of the juvenile lower crust and a small proportion of basement rocks triggered by mantle upwelling in a post-collisional tectonic setting.

Re-melting of the sulfide cumulate residual in the lithospheric mantle and the juvenile lower crust could plausibly provide significant amounts of metals for gold mineralization in the Tian Shan orogeny, following porphyry Cu-Au mineralization during the plate subduction stage. The high initial water content and weakly oxidized to slightly reduced redox state (near FMQ) in the source areas provide an optimum condition for the transport and enrichment of gold in the melt.

Acknowledgments

Appendix A. Supplementary data

Supplementary data associated with this article can be found, in the online version, at https://doi.org/10.1016/j.oregeorev.2018.07.007.

References

Abzalov, M., 2007. Zarmitan granitoid-hosted gold deposit, Tian Shan belt, Uzbekistan. Econ. Geol. 102 (3), 519–532.

Alexeiev, D.V., Cook, H.E., Djenchuraeva, A.V., Mikolaichuk, A.V., 2017. The stratigraphic, sedimentological and structural evolution of the southern margin of the Kazakhstan continent in the Tien Shan Range during the Devonian to Permian. Geol. Soc. Lond. Spec. Publ. 427 (1), 231–269.

Alexeiev, D.V., Kröner, A., Hegner, E., Rojas-Agramonte, Y., Biske, Y.S., Wong, J., Geng, H.Y., Ivleva, E.A., Mühlberg, M., Mikolaichuk, A.V., Liu, D., 2016. Middle to Late Ordovician arc system in the Kyrgyz Middle Tianshan: From arc-continent collision to subsequent evolution of a Palaeozoic continental margin. Gondwana Res. 39, 261–291.

Anderson, J.L., Smith, D.R., 1995. The effects of temperature and fO₂ on the Al-in-hornblende barometer. Am. Mineral. 80 (5–6), 549–559.

Baker, T., Lang, L., 2001. Fluid inclusion characteristics of intrusion-related gold mineralization, Tombstone-Tungsten magmatic belt, Yukon Territory, Canada. Mineralium Deposita, 36: 563–582.Bakirov, A.B., Tagiri, M., Sakiev, K.S., Ivleva, E.A., 2003. The Lower Precambrian rocks in the Tien Shan and their geodynamic setting. Geotectonics 37(5) 368–380.

Ballard, J.R., Palin, M.J., Campbell, I.H., 2002. Relative oxidation states of magmas inferred from Ce(IV)/Ce(III) in zircon: application to porphyry copper deposits of northern Chile. Contrib. Miner. Petrol. 144 (3), 347–364.

Barbarin, B., 1999. A review of the relationships between granitoid types, their origins and their geodynamic environments. Lithos 46 (3), 605–626.

Bierlein, F.P., 2005. Possible intrusion-related gold systems in the western Lachlan orogen, southeast Australia. Econ. Geol. 100, 385–398.

Biske, Y.S., Konopelko, D.L., Seltmann, R., 2013. Geodynamics of late Paleozoic magmatism in the Tien Shan and its framework. Geotectonics 47 (4), 291–309.

Blevin, P.L., 2004. Redox and Compositional Parameters for Interpreting the Granitoid Metallogeny of Eastern Australia: implications for Gold-rich Ore Systems. Resour. Geol. 54 (3), 241–252.

Burtman, V.S., 2015. Tectonics and geodynamics of the Tian Shan in the Middle and Late Paleozoic. Geotectonics 49 (4), 302–319.

Chen, Y., Hu, A., Zhang, G., Zhang, Q., 2000. Precambrian basement age and characteristics of Southwestern Tianshan: Zircon U Pb geochronology and Nd Sr isotopic compositions. Acta Petrologica Sinica 16 (01), 91–98.

Cheng, Z., Zhang, Z., Chai, F., Hou, T., Santosh, M., Turesebekov, A., Nurtaev, B.S., 2017. Carboniferous porphyry Cu-Au deposits in the Almalyk orefield, Uzbekistan: the Sarycheku and Kalmakyr examples. Int. Geol. Rev. 46 (1), 1–20.

Chiaradia, M., Konopelko, D., Seltmann, R., Cliff, R.A., 2006. Lead isotope variations

across terrane boundaries of the Tien Shan and Chinese Altay. Miner. Deposita 41 (5), 411–428.

Cole, A., Wilkinson, J.J., Halls, C., Serenko, T.J., 2000. Geological characteristics, tectonic setting and preliminary interpretations of the Jilau gold-quartz vein deposit, Tajikistan. Mineralium Deposita 35 (7), 600–618.

Defant, M.J., Drummond, M.S., 1990. Derivation of some modern arc magmas by melting of young subducted lithosphere. Nature 347 (6294), 662–665.

Dolgopolova, A., Seltmann, R., Konopelko, D., Biske, Y.S., Shatov, V., Armstrong, R., Belousova, E., Pankhurst, R., Koneev, R., Divaev, F., 2017. Geodynamic evolution of the western Tien Shan, Uzbekistan: insights from U-Pb SHRIMP geochronology and Sr-Nd-Pb-Hf isotope mapping of granitoids. Gondwana Res. 47, 76–109.

Ferry, J.M., Watson, E.B., 2007. New thermodynamic models and revised calibrations for the Ti-in-zircon and Zr-in-rutile thermometers. Contrib. Miner. Petrol. 154 (4), 429–437.

Fielding, I.O.H., Johnson, S.P., Zi, J., Sheppard, S., Rasmussen, B., 2018. Neighbouring orogenic gold deposits may be the products of unrelated mineralizing events. Ore Geol. Rev. 95, 593–603.

Fowler, M.B., Kocks, H., Darbyshire, D.P.F., Greenwood, P.B., 2008. Petrogenesis of high Ba-Sr plutons from the Northern Highlands Terrane of the British Caledonian Province. Lithos 105 (1–2), 129–148.

Fu, B., Page, F.Z., Cavosie, A.J., Fournelle, J., Kita, N.T., Lackey, J.S., Wilde, S.A., Valley, J.W., 2008. Ti-in-zircon thermometry: applications and limitations. Contrib. Miner. Petrol. 156 (2), 197–215.

Goldfarb, R.J., Taylor, R.D., Collins, G.S., Goryachev, N.A., Orlandini, O.F., 2014. Phanerozoic continental growth and gold metallogeny of Asia. Gondwana Res. 25 (1), 48–102.

Gou, L., Zhang, L., Tao, R., Du, J., 2012. A geochemical study of syn-subduction and post-collisional granitoids at Muzhaerte River in the Southwest Tianshan UHP belt, NW China. Lithos 136, 201–224.

Griffin, W.L., Wang, X., Jackson, S.E., Pearson, N.J., O'Reilly, S.Y., Xu, X., Zhou, X., 2002. Zircon chemistry and magma mixing, SE China: In-situ analysis of Hf isotopes, Tonglu and Pingtan igneous complexes. Lithos 61 (3–4), 237–269.

Groves, D.I., Goldfarb, R.J., Santosh, M., 2016. The conjunction of factors that lead to formation of giant gold provinces and deposits in non-arc settings. Geosci. Front. 7, 303–314.

Hart, C.J.R., 2007. Reduced intrusion-related gold systems. Mineral Deposits of Canada: A synthesis of Major deposit types, district metallogeny, the Evolution of geological provinces, and exploration methods. Geol. Assoc. Can. Mineral Deposits Division Spec. Publ. 5, 95–112.

Hart, C.J.R., Mair, J.L., Goldfarb, R.J., Groves, D.I., 2004. Source and redox controls on metallogenic variations in intrusion-related ore systems, Tombstone-Tungsten Belt, Yukon Territory, Canada. Earth Environ. Sci. Trans. R. Soc. Edinburgh 95 (1), 339–356.

Hattori, K.H., Keith, J.D., 2001. Contribution of mafic melt to porphyry copper mineralization: evidence from Mount Pinatubo, Philippines, and Bingham Canyon, Utah, USA. Mineralium Deposita 36 (8), 799–806.

Henry, D.J., 2005. The Ti-saturation surface for low-to-medium pressure metapelitic biotites: Implications for geothermometry and Ti-substitution mechanisms. Am. Mineral. 90 (2–3), 316–328.

Holtz, F., Johannes, W., Tamic, N., Behrens, H., 2001. Maximum and minimum water contents of granitic melts generated in the crust: a reevaluation and implications. Lithos 56 (1), 1–14.

Hou, Z., Zheng, Y., Yang, Z., Rui, Z., Zhao, Z., Jiang, S., Qu, X., Sun, Q., 2013. Contribution of mantle components within juvenile lower-crust to collisional zone porphyry Cu systems in Tibet. Miner. Deposita 48 (2), 173–192.

Hou, Z., Zhou, Y., Wang, R., Zheng, Y., He, W., Zhao, M., Evans, N.J., Weinberg, R.F., 2017. Recycling of metal-fertilized lower continental crust: Origin of non-arc Au-rich porphyry deposits at cratonic edges. Geology 45 (6), 563–566.

Jenchuraeva, R.J., Oakes, B., 2001. The Jerooy Gold Deposit. In: R. Seltmann and R.J. Jenchuraeva, Paleozoic Geodynamics and Gold Deposits in the Kyrgyz Tien Shan. IGCP-373 Field conference in Bishkek and Kyrgyz Tien Shan: 16-25 August 2001 & Pre-meeting Field Trip A5 of the Joint 6th Biennial SGA-SEG meeting in Krakow, Poland, pp. 153–161.

Käßner, A., Ratschbacher, L., Pfänder, J.A., Hacker, B.R., Zack, G., Sonntag, B., Khan, J., Stanek, K.P., Gadoev, M., Oimahmadov, I., 2017. Proterozoic-Mesozoic history of the Central Asian orogenic belt in the Tajik and southwestern Kyrgyz Tian Shan: U-Pb, ⁴⁰Ar/³⁹Ar, and fission-track geochronology and geochemistry of granitoids. Geol. Soc. Am. Bull. 129 (3–4), 281–303.

Kempe, U., Graupner, T., Seltmann, R., de Boorder, H., Dolgopolova, A., Zeylmans Van Emmichoven, M., 2016. The Muruntau gold deposit (Uzbekistan)-A unique ancient hydrothermal system in the southern Tien Shan. Geosci. Front. 7 (3), 495–528.

Konopelko, D., Biske, G., Seltmann, R., Eklund, O., Belyatsky, B., 2007. Hercynian post-collisional A-type granites of the Kokshaal Range, Southern Tien Shan, Kyrgyzstan. Lithos 97 (1–2), 140–160.

Konopelko, D., Seltmann, R., Apayarov, F., Belousova, E., Izokh, A., Lepekhina, E., 2013. U-Pb-Hf zircon study of two mylonitic granite complexes in the Talas-Fergana fault zone, Kyrgyzstan, and Ar-Ar age of deformations along the fault. J. Asian Earth Sci. 73, 334–346.

Konopelko, D., Seltmann, R., Biske, G., Lepekhina, E., Sergeev, S., 2009. Possible source dichotomy of contemporaneous post-collisional barren I-type versus tin-bearing A-type granites, lying on opposite sides of the South Tien Shan suture. Ore Geol. Rev. 35 (2), 206–216.

Konopelko, D., Seltmann, R., Mamadjanov, Y., Romer, R.L., Rojas-Agramonte, Y., Jeffries, T., Fidaev, D., Niyozov, A., 2017. A geotraverse across two paleo-subduction zones in Tien Shan, Tajikistan. Gondwana Res. 47, 110–130.

Konopelko, D., Wilde, S.A., Seltmann, R., Romer, R.L., Biske, Y.S., 2018. Early Permian

intrusions of the Alai range: Understanding tectonic settings of Hercynian post-collisional magmatism in the South Tien Shan, Kyrgyzstan. Lithos 302–303, 405–420.

Konopelko, D.L., Biske, Y.S., Kullerud, K., Seltmann, R., Divaev, F.K., 2011. The Koshrabad granite massif in Uzbekistan: petrogenesis, metallogeny, and geodynamic setting. Russ. Geol. Geophys. 52 (12), 1563–1573.

Kudrin, V.S., Solov'Yev, S.G., Stavinskiy, V.A., Karabdin, L.L., 1990. The gold-copper-molybdenum-tungsten ore belt of the Tien Shan. Int. Geol. Rev. 32 (9), 930–941.

Lang, J., Baker, T., 2001. Intrusion-related gold systems: the present level of understanding. Miner. Deposita 36 (6), 477–489.

Leake, B.E., Woolley, A.R., Arps, C.E., Birch, W.D., Gilbert, M.C., Grice, J.D., Hawthorne, F.C., Kato, A., Kisch, H.J., Krivovichev, V.G., 1997. Nomenclature of Amphiboles: Report of the Subcommittee on Amphiboles of the International Mineralogical Association Commission on New Minerals and Mineral Names. Mineralogical Mag. 61 (2), 295–321.

Li, X., Chi, G., Zhou, Y., Deng, T., Zhang, J., 2017. Oxygen fugacity of Yanshanian granites in South China and implications for metallogeny. Ore Geol. Rev. 88, 690–701.

Long, X., Gao, J., Klemd, R., Beier, C., Qian, Q., Zhang, X., Wang, J., Jiang, T., 2011. Geochemical and geochronological studies of granitoid rocks from the Western Tianshan Orogen: Implications for continental growth in the southwestern Central Asian Orogenic Belt. Lithos 126 (3–4), 321–340.

Long, X., Sun, M., Yuan, C., Kröner, A., Hu, A., 2012. Zircon REE patterns and geochemical characteristics of Paleoproterozoic anatectic granite in the northern Tarim Craton, NW China: Implications for the reconstruction of the Columbia supercontinent. Precambr. Res. 222–223, 474–487.

Loury, C., Rolland, Y., Cenki-Tok, B., Lanari, P., Guillot, S., 2016. Late Paleozoic evolution of the South Tien Shan: Insights from P-T estimates and allanite geochronology on retrogressed eclogites (Chatkal range, Kyrgyzstan). J. Geodyn. 96, 62–80.

Ludwig, K.R., 2003. User's manual for Isoplot 3.00: a geochronological toolkit for. Microsoft Excel. Kenneth R. Ludwig.

Mair, J.L., Farmer, G.L., Groves, D.I., Hart, C.J., Goldfarb, R.J., 2011. Petrogenesis of postcollisional magmatism at Scheelite Dome, Yukon, Canada: evidence for a lithospheric mantle source for magmas associated with intrusion-related gold systems. Econ. Geol. 106, 451–480.

Mao, J., Konopelko, D., Seltmann, R., Lehmann, B., Chen, W., Wang, Y., Eklund, O., Usubaliev, T., 2004. Postcollisional age of the Kumtor gold deposit and timing of Hercynian events in the Tien Shan, Kyrgyzstan. Econ. Geol. 99 (8), 1771–1780.

Martin, H., Smithies, R.H., Rapp, R., Moyen, J.F., Champion, D., 2005. An overview of adakite, tonalite-trondhjemite-granodiorite (TTG), and sanukitoid: relationships and some implications for crustal evolution. Lithos 79 (1–2), 1–24.

Middlemost, E.A.K., 1994. Naming materials in the magma/igneous rock system. Earth Sci. Rev. 37 (3–4), 215–224.

Morelli, R., Creaser, R.A., Seltmann, R., Stuart, F.M., Selby, D., Graupner, T., 2007. Age and source constraints for the giant Muruntau gold deposit, Uzbekistan, from coupled Re-Os-He isotopes in arsenopyrite. Geology 35 (9), 795–798.

Mühlberg, M., Hegner, E., Klemd, R., Pfänder, J.A., Kaliwoda, M., Biske, Y.S., 2016. Late Carboniferous high-pressure metamorphism of the Kassan Metamorphic Complex (Kyrgyz Tianshan) and assembly of the SW Central Asian Orogenic Belt. Lithos 264, 41–55.

Nachit, H., Ibhi, A., Abia, E.H., Ohoud, M.B., 2005. Discrimination between primary magmatic biotites, reequilibrated biotites and neoformed biotites. Comptes rendus-Géoscience 337 (16), 1415–1420.

Nevolko, P.A., Pham, T.D., Tran, T.H., Tran, T.A., Ngo, T.P., Fominykh, P.A., 2018. Intrusion-related Lang Vai gold-antimony district (Northeastern Vietnam): geology, mineralogy, geochemistry and 40 Ar/ 39 Ar age. Ore Geol. Rev. 96, 218–235.

Nikitin, V.I., 1997. Geologycal map of Kassan ore district (1: 25000). State Agency on Geology and Mineral Resources, Kyrgyz Republic.

Nikonorov, V.V., Karaev, Y.V., Borisov, F.I., Tolsky, V.I., Zamaletdinov, T.S., Larina, T.V., Gorbaneva, T.V., 2007. Gold resources of Kyrgyzstan. The Kyrgyz Methodical Expedition for Geological & Economical Research, Bishkek, pp. 500.

Peng, T., Wilde, S.A., Fan, W., Peng, B., 2013. Late Neoarchean potassic high Ba-Sr granites in the Taishan granite-greenstone terrane: petrogenesis and implications for continental crustal evolution. Chem. Geol. 344, 23–41.

Petford, N., Atherton, M., 1996. Na-rich partial melts from newly underplated basaltic crust: the Cordillera Blanca Batholith, Peru. J. Petrol. 37 (6), 1491–1521.

Porter, T.M., 2006. The Tien Shan Belt: Golden Heart of Central Asia. Gangue 88 (1), 4–5.

Rapp, R.P., Watson, E.B., 1995. Dehydration melting of metabasalt at 8–32 kbar: implications for continental growth and crust-mantle recycling. J. Petrol. 36 (4), 891–931.

Richards, J.P., 2009. Postsubduction porphyry Cu-Au and epithermal Au deposits: Products of remelting of subduction-modified lithosphere. Geology 37 (3), 247–250.

Richards, J.P., 2011a. High Sr/Y arc magmas and porphyry Cu ± Mo ± Au deposits: just add water. Econ. Geol. 106 (7), 1075–1081.

Richards, J.P., 2011b. Magmatic to hydrothermal metal fluxes in convergent and collided margins. Ore Geol. Rev. 40 (1), 1–26.

Ridolfi, F., Renzulli, A., Puerini, M., 2010. Stability and chemical equilibrium of amphibole in calc-alkaline magmas: an overview, new thermobarometric formulations and application to subduction-related volcanoes. Contrib. Miner. Petrol. 160 (1), 45–66.

Rowins, S.M., 2000. Reduced porphyry copper-gold deposits: A new variation on an old theme. Geology 28 (6), 491–494.

Seltmann, R., Konopelko, D., Biske, G., Divaev, F., Sergeev, S., 2011. Hercynian postcollisional magmatism in the context of Paleozoic magmatic evolution of the Tien Shan orogenic belt. J. Asian Earth Sci. 42 (5), 821–838.

Seltmann, R., Porter, T.M., Pirajno, F., 2014. Geodynamics and metallogeny of the central Eurasian porphyry and related epithermal mineral systems: a review. J. Asian Earth Sci. 79, 810–841.

Sillitoe, R.H., Bonham, H.F., 1990. Sediment-hosted gold deposits: distal products of magmatic-hydrothermal systems. Geology 18 (2), 157–161.

Smythe, D.J., Brenan, J.M., 2016. Magmatic oxygen fugacity estimated using zircon-melt partitioning of cerium. Earth Planet. Sci. Lett. 453, 260–266.

Solomon, M., 1990. Subduction, arc reversal, and the origin of porphyry copper-gold deposits in island arcs. Geology 18, 630–633.

Solomovich, L.I., 2007. Postcollisional magmatism in the South Tien Shan Variscan Orogenic Belt, Kyrgyzstan: evidence for high-temperature and high-pressure collision. J. Asian Earth Sci. 30 (1), 142–153.

Solomovich, L.I., Trifonov, B.A., 2002. Postcollisional granites in the South Tien Shan Variscan Collisional Belt, Kyrgyzstan. J. Asian Earth Sci. 21 (1), 7–21.

Solomovich, L.I., Trifonov, B.A., 2014. Rapakivi granites within Phanerozoic collisional orogens as a possible consequence of continental subduction and following exhumation of the Precambrian crust: Evidences from the Permian Jangart rapakivi in South Tien Shan collisional belt, Eastern Kyrgyzstan. J. Asian Earth Sci. 96, 332–343.

Sun, W., Huang, R., Li, H., Hu, Y., Zhang, C., Sun, S., Zhang, L., Ding, X., Li, C., Zartman, R.E., Ling, M., 2015. Porphyry deposits and oxidized magmas. Ore Geol. Rev. 65, 97–131.

Tarney, J., Jones, C.E., 1994. Trace element geochemistry of orogenic igneous rocks and crustal growth models. J. Geol. Soc. 151 (5), 855–868.

Taylor, S.R., Mclennan, S.M., 1985. The Continental Crust: Its Composition and Evolution, An Examination of the Geochemical Record Preserved in Sedimentary Rocks. Blackwell Scientific Publications, Surrey, pp. 312.

Thompson, J., Newberry, R.J., 2000. Gold deposits related to reduced granitic intrusions. Rev. Econ. Geol. 13, 377–400.

Turnbull, R., Weaver, S., Tulloch, A., Cole, J., Handler, M., Ireland, T., 2010. Field and Geochemical Constraints on Mafic-Felsic Interactions, and Processes in High-level Arc Magma Chambers: an Example from the Halfmoon Pluton, New Zealand. J. Petrol. 51 (7), 1477–1505.

Wall, V.J., Graupner, T., Yantsen, V., Seltmann, R., Hall, G.C., Muhling, J., 2004. Muruntau, Uzbekistan: a giant thermal aureole gold (TAG) system. In: Muhling, J., et al. (ed.) SEG 2004: Predictive Mineral Discovery Under Cover-Extended Abstracts: Centre for Global Metallogeny. Universiy of Western Australia Publication, pp. 199–203.

Windley, B.F., Alexeiev, D., Xiao, W., Kroner, A., Badarch, G., 2007. Tectonic models for accretion of the Central Asian Orogenic Belt. J. Geol. Soc. 164 (1), 31–47.

Xu, X., Li, X., Ma, Z., Xia, L., Xia, Z., Peng, S., 2006. LA-ICPMS zircon U-Pb dating of gabbro from the Bayingou ophiolite in the northern Tianshan Mountains. Acta Geol. Sin. 80 (8), 1168–1176.

Xue, C., Zhao, X., Mo, X., Dong, L., Gu, X., Nurtaev, B., Pak, N., Zhang, Z., Wang, X., Zu, B., Zhang, G., Feng, B., Liu, J., 2014. Asian Gold Belt in western Tianshan and its dynamic setting, metallogenic control and exploration. Earth Sci. Front. 21 (5), 128–155.

Yakubchuk, A.S., Shatov, V.V., Kirwin, D., Tomurtogoo, O., Badarch, G., Buryak, A.A., 2005. Gold and base metal metallogeny of the Central Asian Orogenic supercollage. Economic geology 100th anniversary 100, 1035–1068.

Yang, X., Lentz, D.R., Sylvester, P.J., 2006. Gold contents of sulfide minerals in granitoids from southwestern New Brunswick, Canada. Mineralium Deposita 41 (4), 369–386.

Zajacz, Z., Candela, P.A., Piccoli, P.M., Wälle, M., Sanchez-Valle, C., 2012. Gold and copper in volatile saturated mafic to intermediate magmas: solubilities, partitioning, and implications for ore deposit formation. Geochim. Cosmochim. Acta 91, 140–159.

Zartman, R.E., Doe, B.R., 1981. Plumbtectonics-the model. Tectonophysics 75 (1), 135–162.